

Anmerkungen zur Simulation von entfestigendem Materialverhalten

Vom Fachbereich Mechanik
der Technischen Universität Darmstadt
zur Erlangung der Lehrbefugnis
für das Fach Mechanik
genehmigte Habilitationsschrift

von

Dr.-Ing. Herbert Baaser
aus
Rüsselsheim / Main
wohnhaft in
Bingen–Büdesheim

1. Gutachter	Prof. Dr.-Ing. D. Gross
2. Gutachter	Prof. Dr.-Ing. Ch. Tsakmakis
Tag der Einreichung	16.05.2003
Tag der Habilitation	30.01.2004

Darmstadt 2004

– D 17 –

Herausgeber:

Institut für Mechanik
Technische Universität Darmstadt
Hochschulstraße 1
64289 Darmstadt

© Herbert Baaser

Alle Rechte, insbesondere das der Übersetzung in fremde Sprachen, vorbehalten.
Ohne Genehmigung des Autors ist es nicht gestattet, dieses Heft ganz oder teilweise
auf photomechanischem, elektronischem oder sonstigem Wege zu vervielfältigen.

ISBN 3-935868-08-1

Vorwort und Dank

Im folgenden gebe ich einen Überblick über die wesentlichen Teile meines Arbeitsgebiets am Institut für Mechanik der TU Darmstadt seit meiner Promotion 1999. Die meisten der hier dargestellten Veröffentlichungen sind in diesem Zeitraum durch meine Tätigkeit direkt in Darmstadt entstanden. Währenddessen war ich im Jahr 2000 für ein halbes Jahr zu Gast bei Prof. Tvergaard in Kopenhagen, Dänemark, und im Laufe der letzten Jahre mehrmals zu Forschungsaufenthalten auf Einladung von Prof. Kuna in Freiberg, Sachsen, innerhalb des dortigen SFB 393. Alle Besuche haben mich auf ihre Weise bereichert und Impulse für die gemeinsame Arbeit gegeben. Stellenweise fließt dies in die Ergebnissen ein, ohne jedesmal explizit erwähnt zu werden. Beiden sei hiermit auch nochmals besonders für das entgegengebrachte Vertrauen, die immerwährende Bereitschaft zu wissenschaftlichen Diskussionen und die erfahrene Gastfreundschaft gedankt.

An dieser Stelle danke ich nochmals meinem wissenschaftlichen Lehrer Prof. Gross, der meine Fähigkeiten auf manchen Gebieten oft wesentlich vor mir selbst erkannt und mich dahingehend gefördert und gefordert hat. Ein weiterer — nicht weniger herzlicher — Dank gilt Prof. Tsakmakis, der gerade in den letzten beiden Jahren sehr oft Ansprech- und Diskussionspartner gewesen ist.

Danke möchte ich aber auch meiner Familie und meinen Eltern sagen. Es ist bestimmt nicht immer einfach mit mir (gewesen), wenn ich mit einem gewissen Drang nach stetiger Erweiterung meiner Programm-Codes und *Erkenntnisgewinn* Stunde um Stunde „abgetaucht“ bin. Trotzdem haben Sie mir immer wieder Kraft und Vertrauen entgegengebracht ...

Zu guter letzt seien an dieser Stelle vor allem die Kollegen Steffen Eckert und Dr.-Ing. Ralf Müller aus der Arbeitsgruppe IV genannt, die immer wieder mindestens ein offenes Ohr für mich haben und inzwischen zu engen Freunden geworden sind.

Inhaltsverzeichnis

I Anmerkungen zur Simulation von entfestigendem Materialverhalten	1
1 Übersicht und Diskussion	3
Eigene Veröffentlichungen	9
2 Ausblick	13
II Diskutierte Veröffentlichungen	15
3 A New Algorithmic Approach treating Nonlocal Effects at Finite Rate-independent Deformation using the Rousselier Damage Model	17
4 Remarks on the Use of Continuum Damage Models and on the Limitations of their Applicability in Ductile Fracture Me- chanics	47
5 Analysis of void growth in a ductile material in front of a crack tip	69
6 The PADÉ–Approximation for Matrix Exponentials Applied to an Integration Algorithm Preserving Plastic Incompressi- bility	83
Verzeichnis der insgesamt zitierten Literatur	103

Teil I

Anmerkungen zur Simulation

von

entfestigendem

Materialverhalten

Kapitel 1

Übersicht und Diskussion

Mit den weiterhin ungebremsten Entwicklungen auf dem Gebiet der *Computer-Hardware* bieten sich für Wissenschaftler und Ingenieure Möglichkeiten der rechnergestützten Simulation in Bereichen, die noch vor wenigen Jahren als unvorstellbar galten.

Der Einsatz von computerbasierten Systemen ist aus keinem Bereich ingenieurtechnischer Forschungs- und Entwicklungsarbeit mehr wegzudenken. Selbst komplizierteste Abläufe in einer langen Prozesskette ausgegehend von ersten Entwürfen, über verschiedene Prototypen hinweg, bis hin zu einem serienreifen Endprodukt werden inzwischen *virtuell* ausgeführt (Stichwort „C-Techniken“: CAD, CAM, CAE, ...). Dies führt zu immer kürzeren Entwicklungszeiten und einem zunehmend kostengünstigeren Entwicklungsablauf¹.

Nicht abzustreiten sind in diesem Zusammenhang die Vorteile, die es mit sich bringt, dass z.B. ein Bauteilkonstrukteur schon in einem sehr frühen Stadium einer aktuellen Entwicklung aus einem *CAD*-System heraus mit einfach zu bedienenden *Finite Elemente*-Programmen erste Analysen hinsichtlich von Tragverhalten oder Bauteilversagen anstellen kann.

Aus Sicht der Strukturmechanik sind einige Materialmodelle, die in irgendeiner Weise einen *Tragfähigkeitsverlust* bzw. *Entfestigung* abbilden können, bereits in kommerziellen FEM-Systemen erhältlich und somit auch in industriellen Anwendungen im Einsatz.

¹Ob diese beiden Faktoren, die an dieser Stelle immer angeführt werden, langfristig der Sache gerecht werden, wird erst die Zukunft zeigen !

Allerdings bringen Materialmodelle dieses Typs eine ganz neue Qualität von möglichen Fehlerquellen zwangsläufig mit in die computergestützte Simulation ein, die ohne spezielle Schulung des Anwenders nicht direkt zu erkennen sind. Später wird auf diesen Punkt speziell näher eingegangen.

In dieser Arbeit sind einige grundsätzliche Aspekte zusammengestellt, die die oben genannten Entwicklungen bestimmt nicht aufhalten können, dennoch aber nicht von untergeordneter Bedeutung sind, weil sie möglicherweise einige Dinge in einem anderen Licht erscheinen lassen.

Aus ingenieurtechnischer Sicht beschränken wir uns in diesem Zusammenhang auf metallische Werkstoffe wie Eisen bzw. Stähle, Aluminium oder Kupfer, die einen kristallinen Aufbau besitzen. Die jeweils vorliegende *Mikrostruktur* hat oftmals einen Einfluss auf das makroskopische Verhalten der Materialien.

Alle hier angegebenen Simulationen gehen von einem *ratenunabhängigen* Materialverhalten aus, wodurch die Zeit t zu einem reinen Lastparameter wird. Somit werden hier mit fortschreitender Zeit monoton ansteigende, globale Belastungen vorgegeben. Sehr wohl kann es aber auch hier zu lokalen Entlastungen kommen.

Diese Voraussetzung schränkt damit zwar die Klasse der diesen Simulationen zugänglichen Materialien ein, reduziert aber gleichzeitig auch den Satz an Parametern, der die Ergebnisse beeinflussen könnte. Eine Diskussion gerade der in dieser Arbeit kritischen Punkte wird somit konzentriert.

Aus Sicht einer numerischen Umsetzung des Werkstoffes wird ebenfalls eine Konzentration auf diese Art von Materialverhalten hervorgehoben, wodurch alle bekannten Versuche von *viskoplastischen* Regularisierungen aussen vor bleiben und damit ebenfalls nicht Diskussionspunkt sein können.

Die in der Literaturliste angegebenen, eigenen Veröffentlichungen lassen sich in vier Gruppen einordnen, welche jeweils eine Forschungsrichtung darstellen. Dafür beispielhaft sollen die folgenden Arbeiten ausgewählt und im Rahmen dieser Habilitation ausführlicher diskutiert werden:

- Die Veröffentlichung BAASER & TVERGAARD [2003] ist aus einer Zusammenarbeit BAASER & TVERGAARD [2000] entstanden und behandelt eine bis dahin neuartige, algorithmische Methode der Integration von Materialmodellen in einem nichtlokalen Sinn am Beispiel des Schädigungsmodells von ROUSSELIER *et al.* [1989].

Die nichtlokale Behandlung von Materialmodellen stellt eine Möglichkeit der *Regularisierung* der Materialgleichungen dar, wobei durch eine Volumenmittelung bestimmter Größen (hier die Schädigungsvariable) eine zusätzliche *charakteristische Länge* ins Problem eingeführt wird.

Mit dieser Methode ist ein Lösungsverhalten zu erreichen, das nahezu von der Diskretisierung unabhängig zu eindeutigen Ergebnissen führt, vgl. hierzu auch BAASER & GROSS [2001a].

Erste Ideen zu dieser Behandlung der Materialgleichungen losgelöst von einer strikten Auswertung auf Integrationspunktebene ist durch die Zusammenarbeit innerhalb des SFB 298² mit O. SCHERF [2000] entstanden.

Ähnliche Ansätze finden sich z.B. in ELLSIEPEN [1999] oder ELLSIEPEN & HARTMANN [2001] und werden inzwischen konsequent durch S. ECKERT in dem von mir initiierten Projekt DAEdalon.org weiter verfolgt, siehe ECKERT *et al.* [2003a] und ECKERT *et al.* [2003b].

- Eine Reihe von Untersuchungen, die sich direkt an die oben besprochene Thematik anschließen, ist ausführlich in BAASER & GROSS [2003b] dargestellt und erstmals in BAASER & GROSS [2001b] vorgestellt worden.

Die numerische Simulation von entfestigendem Materialverhalten z.B. mit Hilfe von Kontinuumsschädigungsmodellen ist ab einem bestimmten Punkt durch Stabilitätsproblem auf der Ebene der Materialformulierung gekennzeichnet.

Im Rahmen den Methode der Finiten Elemente führt diese Eigenschaft unweigerlich zu einem Rangabfall im Beitrag des betreffenden Integrationspunkts zur zugehörigen Elementsteifigkeitsmatrix, was durch das Erreichen eines ersten Nulleigenwerts gekennzeichnet ist.

Durch den Assemblierungsprozess der einzelnen Elementsteifigkeitsmatrizen zur globalen Gesamtsteifigkeit des Systems wird sozusagen eine Verschmierung einzelner Beiträge vorgenommen. Aus diesem Grund kann eine mögliche Instabilität auf einem einzelnen Integrationspunkt nicht zwangsläufig durch eine Analyse der Gesamtsteifigkeitsmatrix detektiert werden. Erst

²Sonderforschungsbereich 298, TU Darmstadt, 1994–2002, „Deformation und Versagen von metallischen und granularen Materialien“

wenn es auf ausreichend vielen Integrationspunkten zu Materialinstabilitäten kommt, die sich gegenseitig nicht mehr „überdecken“ können, ist es möglich einen globalen Steifigkeitsverlust zu erkennen. Damit wird auch einsichtig, dass ein solcher globaler Punkt nicht als Kriterium von Materialinstabilität innerhalb einer Struktur herangezogen werden kann, weil es vorher schon Bereiche lokaler Instabilität gegeben haben muss, die übergangen worden sind. Diese „verschmierende“ Eigenschaft der FEM stellt sich gerade bei der Simulation von entfestigendem Materialverhalten als entscheidender Nachteil dieser Methode heraus und führt zu den in diesem Zusammenhang oft erwähnten Netzabhängigkeit der numerischen Resultate.

Das betrachtete System verliert seine positive Definitheit, der Typ des zu lösenden Differentialgleichungssystems ändert sich (in den betrachteten Fällen verliert es die *Elliptizität* und wird para-/hyperbolisch), mathematisch spricht man von nun an von einer „Schlecht–Gestelltheit“.

Gerade diesen Typwechsel des DGL–Systems versucht man mit entsprechenden, oben erwähnten Regularisierungsmethoden zu vermeiden.

Dennoch stellt ein möglicher Rissfortschritt (Schaffung neuer Oberflächen!) ein Stabilitätsproblem dar, dessen Auftreten / Detektierung numerisch von Interesse ist. Möglicherweise ist man in der Lage, z.B. durch ein räumlich adaptives Verfahren in Verbindung mit der Formulierung einer *Kohäsivzone*, den Rißfortschritt in geeigneter Weise ab diesem Punkt darzustellen, siehe LEPPIN [2000].

Die Auswertung der Determinante des sogenannten *Akustik–Tensors* stellt aus material–theoretischer Sicht (beginnend mit HILL [1958]) eine Möglichkeit dar, das erste lokale Auftreten eines *Null–Eigenwertes* und damit einen Rangabfall/Stabilitätspunkt zu finden. Ein Weiterrechnen über diesen Punkt hinaus, ohne das numerische Werkzeug geeignet zu wechseln, ist aus dieser Sicht sehr fragwürdig und liefert die hinlänglich bekannte *Netzabhängigkeit* der numerischen Resultate.

Eine gleichzeitig zur Lösung des gestellten Randwertproblems mitgeführte Auswertung des akustischen Tensors stellt für den vollen 3D–Fall einen erheblichen numerischen Mehraufwand dar. Dies wird ebenfalls in den Veröffentlichungen zu dieser Thematik diskutiert.

Eine zur Auswertung des Akustik-Tensors alternative Überlegung wird u.a. in PETRYK [1997] dargestellt, ist allerdings für die hier behandelten Fälle noch nicht umgesetzt und untersucht worden.

- In BAASER & GROSS [2001a] wird im Gegensatz zu den beiden oben genannten Arbeiten eine Analyse durchgeführt, deren Blick auf die Kornstruktur der metallischen Werkstoffe gerichtet ist.

In einem Ausschnitt vor einer Rissspitze, die durch ein K -Fernfeld im Rissöffnungsmodus I belastet ist, wird eine durch Zufallsgenerator erzeugte Kornstruktur mit darin enthaltenen diskret verteilten Mikroporen betrachtet. Für diese erste Untersuchung ist eine Inhomogenität im betrachteten Feld durch unterschiedliche Materialkennwerte der Körner untereinander für den Bereich der plastischen Verfestigung erreicht worden.

Über die Deformationsgeschichte hinweg kann man mit diesem Werkzeug Einblicke in das Versagensverhalten beim Zusammenwachsen von Mikroporen erhalten und die wirksamen Mechanismen eindrucksvoll studieren.

U.a. wird deutlich, wie Spannungsüberhöhungen zu Dehnungslokalisierung „im Kleinen“ zwischen den Poren führen. Es lässt sich im weiteren leicht erkennen, wie sich durch Porenvereinigung eine *Makroschädigung* einstellt.

Die dabei entwickelten numerischen Werkzeuge erlauben eine Vielzahl von weitergehenden Detailuntersuchungen auf die im abschließenden Abschnitt nochmals eingegangen werden soll.

Im übrigen kann man diese Entwicklung auch in einen internationalen Rahmen stellen und zur Kenntnis nehmen, dass auch gerade in den USA mit dem Gebiet der *Computational Material Sciences* ein Bindeglied zwischen der klassischen, angewandten Mechanik und den Materialwissenschaften geschaffen wird.

- Die Arbeit BAASER [2004] befasst sich mit einem weiteren Detail der numerischen Umsetzung von kristallinen Materialeigenschaften. Die algorithmische Beschreibung von Einkristallen mit ihren diskreten Gleitebenen stellt aus Sicht der Kontinuumsmechanik immer noch ein Problem dar, weil das Auftreten von Plastizität, hier als irreversibler, ratenunabhängiger Prozess verstanden, mit Abgleitvorgängen auf den durch die Kristallstruktur

gegebenen Gleitebenen identifiziert wird. Schon durch einfache geometrische Überlegungen stellt man fest, dass für bestimmte Deformationen nicht immer alle Gleitebenen *aktiv* sein müssen.

Dieses Verhalten führt auf ein mathematisches Optimierungsproblem mit Ungleichungsnebenbedingungen und muss numerisch gelöst werden.

In neueren Arbeiten wird hierfür ein *augmented-LAGRANGE*-Verfahren angegeben und daraus ein Integrationsalgorithmus abgeleitet.

Die Anwendung eines klassischen EULER-rückwärts-Verfahrens als numerischer Integrationsalgorithmus verletzt aber bekannterweise die Bedingung der *plastischen Inkompressibilität*. Dies führt für den betrachteten Fall von Kristallplastizität zu einem Fehler, der sich von Schritt zu Schritt immer weiter akkumuliert und das Ergebnis verfälscht.

In der vorgestellten Arbeit wird zur Integration ein Exponentialansatz gewählt, der volumenerhaltend ist und der in der numerischen Umsetzung durch eine PADÉ-Approximation dargestellt wird.

Dies führt zu den gewünschten Eigenschaften und zu einem unbedingt stabilen Lösungsverhalten.

Eigene Veröffentlichungen

◊ referiert in wissenschaftlichen Zeitschriften

HOHE, J. , BAASER, H. & GROSS, D. (1996). 'Analysis of ductile crack growth by means of a cohesive damage model'. *International Journal of Fracture* 81, 99–112.

BAASER, H. & GROSS, D. (1998b). Damage and strain localisation during crack propagation in thin-walled shells. *Journal de Physique IV*, 8.

BAASER, H. & GROSS, D. (2000). 'Crack analysis in ductile cylindrical shells using Gurson's model'. *International Journal of Solids and Structures* 37, 7093–7104.

BAASER, H. & GROSS, D. (2001a). '3D Nonlocal Simulation of Ductile Crack Growth — A Numerical Realization'. *European Journal of Finite Elements* 10(2–3–4), 353–367. ISBN 2-7462-0260-3.

BAASER, H. & TVERGAARD, V. (2003). 'A new algorithmic approach treating nonlocal effects at finite rate-independent deformation using the Rousselier damage model'. *Computer Methods in Applied Mechanics and Engineering* 192(1–2), 107–124.

BAASER, H. & GROSS, D. (2003a). 'Analysis of void growth in a ductile material in front of a crack tip'. *Computational Materials Science* 26(C), 28–35.

KOLLING, S. , BAASER, H. & GROSS, D. (2002). 'Material forces due to crack–inclusion interaction'. *International Journal of Fracture*. 18(3), 229–238

BAASER, H. (2004). 'The PADÉ–Approximation for Matrix Exponentials Applied to an Integration Algorithm Preserving Plastic Incompressibility'. *Computational Mechanics*. accepted.

ECKERT, S. , BAASER, H. & GROSS, D. (2003a) 'A DAE–approach applied to elastic–plastic material behavior using FEM' *Z. Angew. Math. Mech.* in press.

ECKERT, S. , BAASER, H. , GROSS, D. & SCHERF, O. (2003b) 'A BDF2 Integration Method with Step Size Control for Elasto–Plasticity' *Computational Mechanics*. submitted and revised.

◊ **Buchbeiträge, Forschungsberichte**

BAASER, H. , HOHE, J. & GROSS, D. (1997). Ductile crack growth analysis using the Gurson damage model. In W. KOSINSKI, R. DE BOER & D. GROSS (Eds.). 'Problems of Environmental and Damage Mechanics'. Instytut Naukowo–Badawczy Zturek. Warszawa, Poland. pp. 139–147.

BAASER, H. & GROSS, D. (1997). Zur Beschreibung des duktilen Rissfortschritts in einem Kreiszylinderrohr. *Forschungs– und Seminarberichte aus dem Bereich der Mechanik der Universität Bochum* S. 71–74. Universität. Bochum.

BAASER, H. & TVERGAARD, V. (2000). A new algorithmic approach treating nonlocal effects at finite rate-independent deformation using the Rousselier damage model. Report DCAMM 647. TU Denmark. Lyngby.

BAASER, H. & GROSS, D. (2003b). Remarks on the use of continuum damage models and on the limitations of their applicability in ductile fracture mechanics. In K. HUTTER & H. BAASER (Eds.). 'Deformation and Failure in Metallic Materials'. Springer.

◊ **Tagungsbeiträge**

BAASER, H. , HOHE, J. & GROSS, D. (1996). Numerische Simulation des duktilen Rißwachstums mit Hilfe eines Streifen–Schädigungsmodells. In '28. Tagung des DVM–Arbeitskreises Bruchvorgänge'. Vol. 228. DVM, Berlin. pp. 189–198. ISSN 0943-3474.

BAASER, H. & GROSS, D. (1999). 3D–Simulation des duktilen Rißwachstums. In '31. Tagung des DVM–Arbeitskreises Bruchvorgänge'. DVM, Berlin. pp. 99–108.

BAASER, H. & GROSS, D. (1998a). 3D–Simulation of Ductile Crack Growth. In A. CARPINTERI & C.A. BREBBIA (Eds.). 'Damage and Fracture Mechanics'. Computational Mechanics Publications. Bologna, Italy. and Proceedings of BETECH99, pp. 587–596.

- BAASER, H. & GROSS, D. (2001b). Ductile damage and crack growth analysis in 3D structures — limitations of CDM approaches. In 'Proceedings of the ICF10'. Hawaii.
- BAASER, H. & GROSS, D. (2002a). A comparative study on the limitations of damage models in ductile fracture mechanics. In 'Proceedings of the CanCNSM 2002'. Vancouver.
- BAASER, H. & GROSS, D. (2002b). On the limitations of CDM approaches to ductile fracture problems. In M.A. MANG, F.G. RAMMERSTORFER & J. EBERHARDSTEINER (Eds.). 'Proceedings of the Fifth World Congress on Computational Mechanics (WCCM V)'. Vienna University of Technology, Austria. Invited Paper.

◇ **Dissertation**

- BAASER, H. (1999). Dreidimensionale Simulation duktiler Schädigungsentwicklung und Rißausbreitung. Dissertation. Technische Universität Darmstadt. Institut für Mechanik.

◇ **Buch**

- HUTTER, K. & BAASER, H. , Eds. (2003). *Deformation and Failure in Metallic Materials. Lecture Notes in Applied and Computational Mechanics*, Vol. 10. Springer.

Kapitel 2

Ausblick

Wie bereits in der vorgegangenen Übersicht und Diskussion zu erkennen sein sollte, werden in dieser Arbeit zumindest vier Richtungen von substanzialen Untersuchungen bei der rechnergestützten Betrachtung von Entfestigungsprozessen angestossen. Auf allen vier Teilgebieten sind wesentliche Fortschritte im grundsätzlichen Verständnis aber auch der konkreten numerischen Umsetzung erzielt worden. Damit sollte man sich keineswegs zufrieden geben, sondern vielmehr angeregt sein, bestgimmte Gedankengänge fortzusetzen und gegebenenfalls die algorithmische Umsetzung weiter zu optimieren.

Neben den hier direkt aufgezeigten vier Entwicklungsmöglichkeiten gibt es aber auch — je nach Blickwinkel — bestimmt noch weitere die hier keine Beachtung gefunden haben.

In diesem Zusammenhang verweise ich an dieser Stelle explizit auf Forschungsaktivitäten in der Arbeitsgruppe von Prof. Kuna, TU BA Freiberg, wo verschiedene Möglichkeiten einer *Parameteridentifikation* speziell für Schädigungsmodelle entwickelt werden. Diese Thematik einer eindeutigen Bestimmung von Materialkennwerten für Schädigungsmodelle ist ein weiteres Betätigungsfeld, das in dieser Arbeit vollständig ausgeklammert bleiben musste, allerdings für zukünftige Entwicklungen unabdingbar ist. Dabei stellen sich ebenfalls Fragen der Eindeutigkeit und inversen Problemlösung, die wegen ihrer Komplexität heute noch garnicht komplett gelöst werden können.

Aus diesem Grund scheinen Zugänge, die mikroskopische Aspekte der Materialstruktur mit makroskopischen Eigenschaften in Verbindung bringen („Homogenisierung“) und daraus eine Parameterbestimmung für Kontinuumsmodelle ermöglichen, unabdingbar und speziell für die Anwendung bei Schädigungsmodellen vielversprechend. Damit sei zum Abschluss auch wiederum der Bogen zum „Werkzeugkasten“ BAASER & GROSS [2003a] geschlagen ...

Teil II

Diskutierte Veröffentlichungen

Kapitel 3

**A New Algorithmic Approach
treating Nonlocal Effects at
Finite Rate-independent
Deformation using the
Rousselier Damage Model**

**COMPUTER METHODS IN APPLIED
MECHANICS AND ENGINEERING,
192 (1–2), 107–124, 2003**

A new algorithmic approach treating nonlocal effects at finite rate-independent deformation using the ROUSSELIER damage model

H. BAASER*, V. TVERGAARD

Department of Solid Mechanics, Technical University of Denmark
DK-2800 Kgs. Lyngby, Denmark

Abstract: *The aim of this contribution is a demonstration of a new iterative approach for the algorithmic treatment of a nonlocal damage formulation in the scope of the finite element method. The damage model of ROUSSELIER is used in a finite strain formulation to represent the material behaviour in the specimens of interest. The new method uses a set of constitutive equations with a BAŽANT-type nonlocal regularisation. An iterative NEWTON–RAPHSON-scheme is applied, which requires the determination of the global stiffness and residuum of the system by the assembling of local solutions at every integration point many times during an iteration loop. The numerical treatment is held in a general form and a three-dimensional example is used to illustrate the performance of this method in comparison with the classical local approach. To effectively represent the shear band localization 20-nodes-brick elements with $2 \times 2 \times 2$ -integration are used.*

Keywords: Ductile Damage, Nonlocal Regularization, 3D–Finite–Element–Simulation, Shear Band Localization

**On leave from:* Institute of Mechanics, Darmstadt University of Technology
Hochschulstr. 1, D–64289 Darmstadt, Germany

Correspondence: baaser@mechanik.tu-darmstadt.de

3.1 Introduction

A well-known disadvantage in the numerical treatment of solid mechanics problems, where softening material behaviour occurs, is the so-called *mesh-dependence* of numerical results. Formulating a physical problem in the form of differential equations and discretizing them for example by the finite element method to obtain a numerical solution one gets results which depend on the chosen finite element mesh if the system of equations loses *ellipticity*. If standard elastic or inelastic constitutive equations are applied, with associated evolution equations for the set of internal variables, the described critical situation is not reached as long as the material remains *stable* in the sense of HILL [1958]. However, when a slightly more difficult material law is used, involving *damage* effects as a special application of inelastic/plastic behaviour, material stability and consequently ellipticity of the global system of equations is not guaranteed. Thus one could get mesh-dependent results because of a local strain-softening effect (for example near a crack tip), although the global structure seems to be in a stable regime indicated by an overall hardening behaviour for the full specimen.

Many articles have introduced different methods to overcome the mesh-dependence of finite element results. The common idea is the implementation of a *characteristic* or *internal* length (scale) into the constitutive model or its evaluation. Some authors try to interpret this additional parameter as material dependent, others declare it as structure or loading dependent. We shall mention four different types of models. A type of COSSERAT model follows the idea of considering in addition to the displacement of a material point also its rotation in the continuum description, see DE BORST [1991] or EHLERS *et al.* [1998]. The internal length introduced was shown to determine the width of shear bands especially in soil materials, where the additional rotational degrees of freedom are activated during the deformation history. For such shear dominated problems this method seems to be a valid regularization technique. Another advanced regularization method is the introduction of the higher gradients of displacements as additional degrees of freedom. These models, generally known as gradient-dependent plasticity models, require also extra degrees of freedom per node in the finite element formulation. A

consistent formulation in terms of small-strain conditions is available, see e.g. DE BORST *et al.* [1999].

A totally different approach to the modeling of failure occurrence is the discrete representation of the actual failure or damage mode. Such models are able to represent the failure occurrence by special finite elements either capable of showing displacement jumps internally within the element structure, see OLIVER [1996], or between the element edges throughout a special *cohesive* law defining the stress-strain behaviour, see e.g. HOHE *et al.* [1996] or BAASER *et al.* [1997].

The last type of regularizing approaches is known as *non-local* based on a spatial smoothing of certain quantities over the volume or structure of interest, see BAŽANT & PIJAUDIER-CABOT [1988]. The main goal of this type of model is an additional evaluation of a volume integral for the internal variables like plastic strain or damage, convoluted e.g. by a bell-like kernel function, see PIJAUDIER-CABOT & BENALLAL [1993]. Many authors used this smoothing technique like LEBLOND *et al.* [1994], TVERGAARD & NEEDLEMAN [1997] or BAASER & GROSS [1998] and computed the smoothing of e.g. the damage parameter as an additional process to the actual result of the evaluation of the set of constitutive equations. This in the sense of the algorithm explicit smoothing procedure causes some problems with the convergence of the numerical solution because it is a disturbance of the former calculated result of the respective smoothed quantity. To overcome this special problem TVERGAARD & NEEDLEMAN [1995] have introduced the quotient $K = \dot{f}/\dot{f}_{local}$ to prevent numerical problems considering GURSON's damage model. They report that the "time step size needs to be small enough so that K at any integration point does not vary substantially from step to step".

In this present paper we follow a new idea of evaluating the volume integral for the increment of the damage parameter used. The idea is to compute the smoothing during the iteration of the set of constitutive equations, which is advantageous due to the iterative character of the equation solver applied. We discuss this approach in detail in Section 3.2.3. The algorithmic treatment is described in Section 3.4.2. A numerical example is shown in Section 3.5 for a typical shear band localization. In this study 20-noded brick 3D

elements are used with quadratic shape functions along the element edges. For this element type MATHUR *et al.* [1994] have found good representation of localization in the 3D case. Another possibility would be the enhanced type 3D elements by SIMO & ARMERO [1992], but this would require big numerical effort in coding and computation.

As constitutive model we use in this paper the ductile damage model of ROUSSELIER *et al.* [1989]. Many numerical investigations of ductile failure by the nucleation and growth of micro–voids have been based on the GURSON model, e.g. see TVERGAARD [1989]. Here, however, we use the ROUSSELIER model to get more experience with predictions of this model. An advantage of this model is that the material softening behaviour due to damage is described by the influence of just three material parameters, according to the chosen formulation. There are a few articles treating the calibration of the ROUSSELIER parameters to experimental data, see ROUSSELIER *et al.* [1989] and LI *et al.* [1994]. A second advantage is related to the numerical implementation of the constitutive law by means of an implicit integration scheme. The type of constitutive equations leads to symmetric tangent material moduli, which is advantageous in computing and storing the matrix expressions. The numerical treatment and integration of this model is described in Section 3.3.2. Additionally we have added in Appendix 3.7 a comprehensive description of the integration procedure of this damage model, including the local derivatives needed to construct an implicit integration scheme.

3.2 The nonlinear solution procedure

Iterative numerical procedures are often used to solve structural problems, when the governing system of differential equations is nonlinear due to the material behaviour and/or the geometry, e.g. caused by large displacements. To get an approximation to the real nonlinear behaviour of the structure considered, the final load, leading to an unknown displacement result \mathbf{u} , is divided in smaller load steps. Thus, for every load level the structural response is computed by finding the actual equilibrium, using an iterative solution procedure. The accumulation of the incremental solutions $\Delta\mathbf{u}$ of the displacement field results in the total answer \mathbf{u} .

3.2.1 Outline of the classical iterative solution procedure

Starting from the weak form of equilibrium $g(\mathbf{u}, \delta\mathbf{u}) = 0$, resulting from the momentum balance equation, an iterative solution method can be constructed to solve for the unknown displacements \mathbf{u} at a given load, with prescribed boundary displacements $\bar{\mathbf{u}}$ on the system. The displacements describe the difference between the current and the initial configuration by $\mathbf{u} = \mathbf{x} - \mathbf{X}$. The representation of $g(\mathbf{u}, \delta\mathbf{u}) = 0$ in terms of a TAYLOR-series from a known position $\hat{\mathbf{u}}$ with $\Delta\mathbf{u} = \mathbf{u} - \hat{\mathbf{u}}$ leads to a first order approximation of the weak form. This expression is the basis for the *global* iteration loop to find the increments $\Delta\mathbf{u}$ and thus the new displacements \mathbf{u} . This procedure is schematically described in Fig. 3.1. In the next load step the new solution of the system has to be determined by repeating this iteration.

3.2.2 The nonlocal formulation

For static and time-independent boundary value problems in solid mechanics the governing differential equations are usually *elliptic*. For such structural analysis there is a large number of efficient numerical algorithms of engineering interest, including inelastic material behaviour.

Problems arise when strain softening material behaviour is modeled, since then the governing differential equations become hyperbolic. A material reaching the softening regime passes a stability point, which results in *mesh dependent* responses when a standard numerical discretizing method is applied.

In the usual iterative procedures all quantities are stored locally on the level of integration points. However, the nonlocal approach to be presented here manipulates the results for the increment of the damage parameter by a smoothing technique and influences through that one internal quantity on the integration points. BAŽANT & PIJAUDIER-CABOT [1988] have shown that a nonlocal treatment of the damage quantities leads to mesh-insensitivity. Other quantities can still be handled in a local way. For this reason we apply the nonlocal smoothing integral to the increment $\Delta\beta$ of ROUSSELIERs

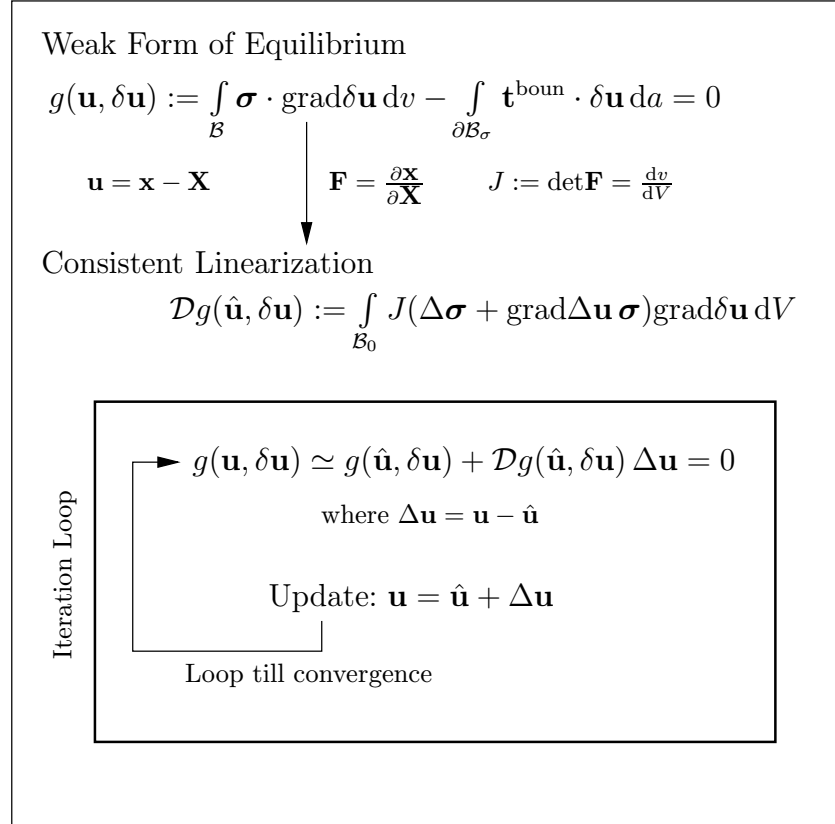


Figure 3.1: Classical Iterative FEM Solution Procedure for a given Load Level

damage quantity

$$\Delta\beta^{nonloc}(\mathbf{x}) = \frac{\int \Delta\beta^{local}(\mathbf{s}) \varphi(\mathbf{s} - \mathbf{x}) d\Omega(\mathbf{s})}{\int \varphi(\mathbf{s} - \mathbf{x}) d\Omega(\mathbf{s})} \quad (3.1)$$

where the kernel function chosen as

$$\varphi(\mathbf{x}) = \exp \left[-\frac{k^2}{l_c^2} \mathbf{x} \cdot \mathbf{x} \right] \quad (3.2)$$

is responsible for the nonlocal smoothing of the local quantity $\Delta\beta^{local}$. The damage model will be described in more detail in section 3.3.2. From a mathematical point of view the characteristic length l_c describes the standard

deviation of the normal distribution (see BAŽANT & PIJAUDIER-CABOT [1988] for a discussion of the factor k depending on the dimension of the problem considered). Following their arguments $k \equiv (6\sqrt{\pi})^{1/3} \simeq 2.2$ for the 3D case considered here.

3.2.3 The new / modified solution algorithm

The focus of the new solution algorithm is on the assembling of the global stiffness matrix and the global residual vector. In Fig. 3.1 the global equilibrium iteration is illustrated, with the use of the residual(vector) $g(\mathbf{u}, \delta\mathbf{u})$ and the actual system stiffness(matrix) $\mathcal{D}g(\hat{\mathbf{u}}, \delta\mathbf{u})$. During the assembling procedure for these terms the actual increments for the local description of the constitutive behaviour are computed. The numerical procedure for this modification is described in detail in Appendix 3.7 (see eqn. (3.28)) where the calculation of the local solution of the constitutive equations is demonstrated. The new idea is a *global* computation of the increments $\Delta\mathbf{x}$ in (3.28) by an iterative LANCZOS solver. The specific algorithmic treatment of this iteration is described in Section 3.4.2. Due to the iterative character of the new solution scheme we are able to modify the actual solution of the increment of the damage parameter β by a *nonlocal* approach, as shown in the previous section. This modification is not possible in the traditional iterative solution procedure, where the evaluation of the constitutive equations is treated in every integration point violating the yield condition, without considering its spatial position.

The here described nonlocal modification of the increment $\Delta\beta$ of the damage parameter can be interpreted as semi-implicit procedure evaluating the set of constitutive equations incorporating the convolution of (3.1). This guarantees the global quadratic convergence behaviour.

3.3 Finite Strain Plasticity and Damage Model

3.3.1 Finite Strain Plasticity

In elastic–plastic solids under sufficiently high load finite deformations occur, where the plastic part of the strains usually is large compared with the elastic part. The description of finite plastic deformations in conjunction with damage models is often done by using the additive decomposition of the elastic and plastic strains rates, TVERGAARD [1989]. Here, however, we use the framework of multiplicative elastoplasticity which is widely accepted in the field. Its kinematic key assumption is the multiplicative split of the deformation gradient

$$\mathbf{F} = \mathbf{F}_{el} \cdot \mathbf{F}_{pl} \quad (3.3)$$

into an elastic and a plastic part, providing the basis of a geometrically exact theory and avoiding linearization of any measure of deformation. As a further advantage, fast and numerically stable iterative algorithms, proposed and described in WEBER & ANAND [1990] or SIMO [1992], can be used. In the following, only a brief summary of the algorithm in the context of a FE–implementation is given.

An essential aspect of (3.3) is the resulting additive structure of the current logarithmic principal strains within the return mapping scheme

$$\boldsymbol{\epsilon}^{el} = \boldsymbol{\epsilon}^{tr} - \Delta\boldsymbol{\epsilon}^{pl}. \quad (3.4)$$

Here, $\epsilon_i = \ln \lambda_i$ ($i = 1, 2, 3$) and λ_i^2 are the eigenvalues of the left CAUCHY–GREEN tensor \mathbf{b}_{el}^{tr} , which describes the elastic trial state. The elastic strains $\boldsymbol{\epsilon}^{el}$ are defined by Hooke’s law and the plastic strain corrector $\Delta\boldsymbol{\epsilon}^{pl}$ can be derived by the normality rule of plastic flow. The elastic left CAUCHY–GREEN tensor can be specified with the decomposition (3.3) as

$$\mathbf{b}_{el} = \mathbf{F}_{el} \cdot \mathbf{F}_{el}^T = \mathbf{F} \cdot \mathbf{C}_{pl}^{-1} \cdot \mathbf{F}^T, \quad (3.5)$$

which clearly shows the “connection” between the elastic and plastic deformation measure by the occurrence of the plastic right CAUCHY–GREEN tensor

$$\mathbf{C}_{pl} = \mathbf{F}_{pl}^T \cdot \mathbf{F}_{pl}.$$

By means of the relative deformation gradient (see SIMO [1992])

$$\mathbf{f} = \frac{\partial \mathbf{x}}{\partial \mathbf{x}_{n-1}} = \mathbf{F} \cdot \mathbf{F}_{n-1}^{-1}, \quad (3.6)$$

which relates the current configuration \mathbf{x} to the configuration belonging to the previous time step at t_{n-1} , an elastic *trial*-state is calculated for the current configuration at time t_n

$$\mathbf{b}_{el}^{tr} = \mathbf{f} \cdot \mathbf{b}_{n-1} \cdot \mathbf{f}^T \quad (3.7)$$

with frozen internal variables at state t_{n-1} . If the condition $\Phi \leq 0$ (see eqn. (3.10)) is fulfilled by the current stress state $\boldsymbol{\tau}$, this state is possible and is the solution. If, on the other hand, $\Phi \leq 0$ is violated by the trial-state, the trial stresses must be projected back on the yield surface $\Phi = 0$ in an additional step. This “return mapping” procedure is used as the integration algorithm for the constitutive equations described in Section 3.3.2. It should be mentioned that the algorithmic treatment in terms of principal axes has some advantages concerning computational aspects like time and memory saving. Based on this, the integration procedure of the constitutive equations for large and for small deformations is very similar, ARAVAS [1987].

3.3.2 The ROUSSELIER Damage Model

Some notations and characters, which will be used in this description of the constitutive law and later on in the algorithmic setting, are specified first. Following the ideas of ARAVAS [1987] we decompose the stress and strain tensors in scalar values, which is also a great advantage for the numerical implementation. Thus, we write the KIRCHHOFF stress tensor $\boldsymbol{\tau}$ as weighted CAUCHY stress tensor in the following way:

$$\boldsymbol{\tau} = J \boldsymbol{\sigma} = -p\mathbf{1} + \frac{2}{3}q\mathbf{n}, \quad (3.8)$$

where $p = -\frac{1}{3}\tau_{ij}\delta_{ij}$ defines the hydrostatic pressure, $q = \sqrt{\frac{3}{2}t_{ij}t_{ij}}$ the equivalent stress and $t_{ij} = \tau_{ij} + p\delta_{ij}$ are the components of the stress deviator. In this notation an additional important value is the normalized stress deviator

$\mathbf{n} = \frac{3}{2q}\mathbf{t}$. The second order identity tensor $\mathbf{1}$ is defined as the KRONECKER symbol by its components δ_{ij} in the cartesian frame. In an analogous way the plastic strain rate can be written as

$$\Delta\boldsymbol{\epsilon}^{pl} = \frac{1}{3}\Delta\varepsilon_p\mathbf{1} + \Delta\varepsilon_q\mathbf{n}, \quad (3.9)$$

where $\Delta\varepsilon_p$ and $\Delta\varepsilon_q$ describe scalar rate quantities which are defined later on. The constitutive model used in this study is the damage model proposed by ROUSSELIER *et al.* [1989]. Here, the yield function taking ductile damage processes into account is written as

$$\Phi = q - \sigma_0 \underbrace{\left[\frac{\varepsilon_{eqv}^{pl}}{\sigma_0} E + 1 \right]}_{\sigma^*}^{1/N} + B(\beta)D \exp\left(-\frac{p}{\sigma_1}\right) = 0, \quad (3.10)$$

where σ^* represents the material hardening in terms of a power law, and the last part of (3.10) represents the damage (softening) behaviour by the function $B(\beta)$ and an exponential assumption. Furthermore, YOUNGS modulus is defined by E , the initial yield stress by σ_0 , the material hardening by the exponent N ; and D and σ_1 are *damage* material parameters. The function $B(\beta)$ is the *conjugate force* to the damage parameter β (see ROUSSELIER *et al.* [1989]), defined by

$$B(\beta) = \frac{\sigma_1 f_0 \exp(\beta)}{1 - f_0 + f_0 \exp(\beta)}. \quad (3.11)$$

Here, the initial void volume fraction f_0 is the third damage depending material parameter used in this set of constitutive equations.

The set of constitutive equations is complemented by the evolution equations for the plastic strain ε_{eqv}^{pl} and the damage parameter β .

The macroscopic plastic strain rate $\dot{\boldsymbol{\epsilon}}^{pl}$ is determined by the classical associated flow rule

$$\dot{\boldsymbol{\epsilon}}^{pl} = \lambda \frac{\partial \Phi}{\partial \boldsymbol{\tau}} = \lambda \left\{ \frac{\partial \Phi}{\partial q} \frac{\partial q}{\partial \boldsymbol{\tau}} + \frac{\partial \Phi}{\partial p} \frac{\partial p}{\partial \boldsymbol{\tau}} \right\}. \quad (3.12)$$

Notice that $\dot{\boldsymbol{\epsilon}}^{pl}$ coincides with the plastic increment $\Delta\boldsymbol{\epsilon}^{pl}$ for the algorithmic setting in (3.4) if it is written in principal axes. The last part of (3.12) shows

a further advantage of this formulation following ARAVAS [1987], because of the very easy determination of the derivatives of Φ with respect to the scalar quantities q and p . One can see with (3.9) and (3.12) that

$$\Delta\varepsilon_p = -\lambda \frac{\partial\Phi}{\partial p} \quad \text{and} \quad \Delta\varepsilon_q = \lambda \frac{\partial\Phi}{\partial q} \quad (3.13)$$

are valid. These two equations allow for the algebraic elimination of the factor λ if

$$\Delta\varepsilon_p \frac{\partial\Phi}{\partial q} + \Delta\varepsilon_q \frac{\partial\Phi}{\partial p} = 0 \quad (3.14)$$

is fulfilled. Thus, the increment of the plastic strain can be expressed by the two scalar quantities $\Delta\varepsilon_p$ and $\Delta\varepsilon_q$. Then the equivalent plastic strain ε_{eqv}^{pl} can be incremented directly by $\Delta\varepsilon_q$.

The evolution equation for the damage parameter β is given by

$$\Delta\beta = \Delta\varepsilon_q D \exp\left(-\frac{p}{\sigma_1}\right) \quad (3.15)$$

which is obviously dependent on the deviatoric part of the strain rate $\Delta\varepsilon_q$ and the current hydrostatic pressure p .

Now the whole set of constitutive equations is known. The evaluation of the material model for a given load level requires the solution of the three equations (3.10), (3.14) and (3.15) for the unknowns $\Delta\varepsilon_p$, $\Delta\varepsilon_q$ and $\Delta\beta$, respectively. *Classically* this evaluation would be done pointwise on the local level in the integration points by an implicit EULER backward integration rule, which is described in detail in Appendix 3.7. In Section 3.2.3 we discuss a new approach, which allows for a nonlocal formulation, and its algorithmic treatment is shown in Section 3.4.2.

The exact linearization of this set of equations follows the description in ARAVAS [1987]. At this point we just mention the starting point of the linearization

$$\boldsymbol{\tau} = \mathbf{C} : \left(\boldsymbol{\epsilon}^{tr} - \frac{1}{3} \Delta\varepsilon_p \mathbf{1} - \Delta\varepsilon_q \mathbf{n} \right), \quad (3.16)$$

where \mathbf{C} is the matrix of the elastic moduli defined by the LAMÉ constants. The variational expression for (3.16) is found as

$$\delta\boldsymbol{\tau} = \mathbf{C} : \left(\delta\boldsymbol{\epsilon}^{tr} - \frac{1}{3} \delta\Delta\varepsilon_p \mathbf{1} - \delta\Delta\varepsilon_q \mathbf{n} - \Delta\varepsilon_q \frac{\partial\mathbf{n}}{\partial\boldsymbol{\tau}} : \delta\boldsymbol{\tau} \right). \quad (3.17)$$

Some extended algebraic manipulations on (3.17), as described in ARAVAS [1987], lead to the expressions $\delta\Delta\varepsilon_p$ and $\delta\Delta\varepsilon_q$ and finally

$$\mathbf{D} = \left(\frac{\partial \boldsymbol{\tau}}{\partial \boldsymbol{\epsilon}} \right)_{t+\Delta t}, \quad (3.18)$$

which is the material modulus for the implicit integration procedure at the end of the time interval $[t, t + \Delta t]$ considered.

The following points explain details of the constitutive model:

1. It is reminded that the current value of the void volume fraction f can be attained by $f = \frac{B(\beta)}{\sigma_1}$ to get a comparison to other damage models, like TVERGAARD [1989].
2. The yield function (3.10) can be seen as classical yield condition of VON MISES plasticity with the hardening function $\sigma^*(\varepsilon_{eqv}^{pl})$ expanded by a third term responsible for the material softening.
3. Note that for a vanished initial void volume fraction $f_0 \equiv 0$ the yield condition (3.10) indicates a VON MISES yield condition without any influence of damage, but in that case no increase of the damage quantity β will take place. This is in contrast to common formulations of GURSON's damage model, where a nucleation of microvoids is especially considered by an additional term to the evolution equation of the void volume fraction f , see TVERGAARD [1989]. The constitutive formulation used here describes "damage" by the parameter β , which has no direct correlation to a measureable quantity. So no special term for the nucleation of microvoids is assumed. With $f_0 \equiv 0$ there will be no influence of eqn. (3.15) on (3.11) and (3.10). Furthermore the algebraic reformulation of (3.13) into (3.14) will break down because of the vanishing derivation $\frac{\partial \Phi}{\partial p}$ in (3.13)₁. With that numerically based argumentation it is necessary to define at least a very small initial void volume fraction f_0 to get an evolution of the damage parameter β .

3.4 Finite Element Formulation

3.4.1 3D–Element

The starting point is the weak form of equilibrium $g(\mathbf{u}, \delta\mathbf{u})$, see Fig. 3.1, formulated in the current configuration, where \mathbf{u} is the displacement and \mathbf{t}_L are the prescribed tractions acting on the boundary $\partial\mathcal{B}_\sigma$ of the body \mathcal{B} . Linearization with respect to the current deformation state, and rearrangement leads (with $d\mathbf{v} = J dV$) to the following representation of the element stiffness

$$Dg^{elmt}(\hat{\mathbf{u}}, \delta\mathbf{u}) = \int_{\mathcal{B}_0} J (\Delta\boldsymbol{\sigma} + \text{grad}\Delta\mathbf{u} \cdot \boldsymbol{\sigma}) \cdot \text{grad} \delta\mathbf{u} \, dV^{elmt} \quad (3.19)$$

where $J = \det \mathbf{F}$ and \mathcal{B}_0 denotes the reference configuration. As for the global residuum vector resulting from $g(\mathbf{u}, \delta\mathbf{u})$ the element results from (3.19) are assembled to the global stiffness matrix \mathbf{K} . For further explanations on the implementation of the consistent linearization of the algorithm used see SIMO [1992] and the modifications in REESE & WRIGGERS [1997] concerning the determination of the eigenvalue decomposition.

The discretization chosen in this paper is based on a 20–node–displacement element formulation with shape functions N_i , ($i = 1, 2, \dots, 20$), so that quadratic functions describe the element edges. These shape functions are constructed in a straightforward manner, see e.g. hints in COOK *et al.* [1989].

As in MATHUR *et al.* [1994] we use a $2 \times 2 \times 2$ integration scheme, which means an *underintegration* with respect to the quadratic shape functions N_i . We point out that again no *hourgassing* mode was detected like that found in the case of an 8–node–displacement element formulation and a $1 \times 1 \times 1$ integration scheme, see BAASER & GROSS [1998].

3.4.2 The algorithmic treatment of the new solution approach

As described above, the iterative solution procedure used for solving non-linear problems by the finite element method requires an evaluation of the constitutive equations on the level of the integration points. This is known as

the lowest level of iteration in contrast to the global load/time incrementation and the subsequent *global* iteration fulfilling the weak form of equilibrium. In our new approach the originally *local* evaluation of the set of constitutive equations on every integration point is shifted from the lowest level to a *global* solution while assembling the system stiffness matrix and the right hand side residual vector.

Instead of solving iteratively for every element integration point, we assemble a large system of equations where the set of equations from every integration point enters blockwise along the main diagonal of the new system matrix. For the case that all integration points are in the inelastic regime, we get the global maximum number of constitutive equations

$$n_{glb}^{const} = n_{loc}^{const} \cdot n_{int}^{elmt} \cdot n_{elem}, \quad (3.20)$$

where n_{loc}^{const} is the local number of constitutive equations (in the present formulation of the ROUSSELIER model $n_{loc}^{const} \equiv 3$), n_{int}^{elmt} is the number of integration points per element (in our case $n_{int}^{elmt} \equiv 8$) and n_{elem} is the current number of elements of the FE-discretization. This maximum number n_{glb}^{const} decreases with the number of integration points staying in the elastic regime, which is distinguished by the yield condition (3.10).

The system matrix is just filled blockwise along the main diagonal with a band of the three equations from the constitutive set and is non-symmetric. It is stated, that the coupling between the integration points within one element or its neighbourhood is defined by the convolution in (3.1) and do not effect the non-main diagonal entries of the supermatrix. This situation is illustrated in Fig. 3.2. The global iteration scheme to find the current equilibrium requires in every iteration loop the assembling of the (global) system matrix and the right hand side vector. Parallel to this assembling procedure, we solve the new global system of constitutive equations by an iterative LANCZOS solver. The algorithm for the LANCZOS solver is shown in Appendix 3.8. The use of the slightly more complicated LANCZOS solver instead of an ordinary conjugated-gradient-solver is chosen due to the possibility that the system matrix is not positive definite, which is not required by the LANCZOS solver. That iterative solution technique is advantageous because of the possible sparse storing technique for the system matrix of Fig. 3.2. Therefore,

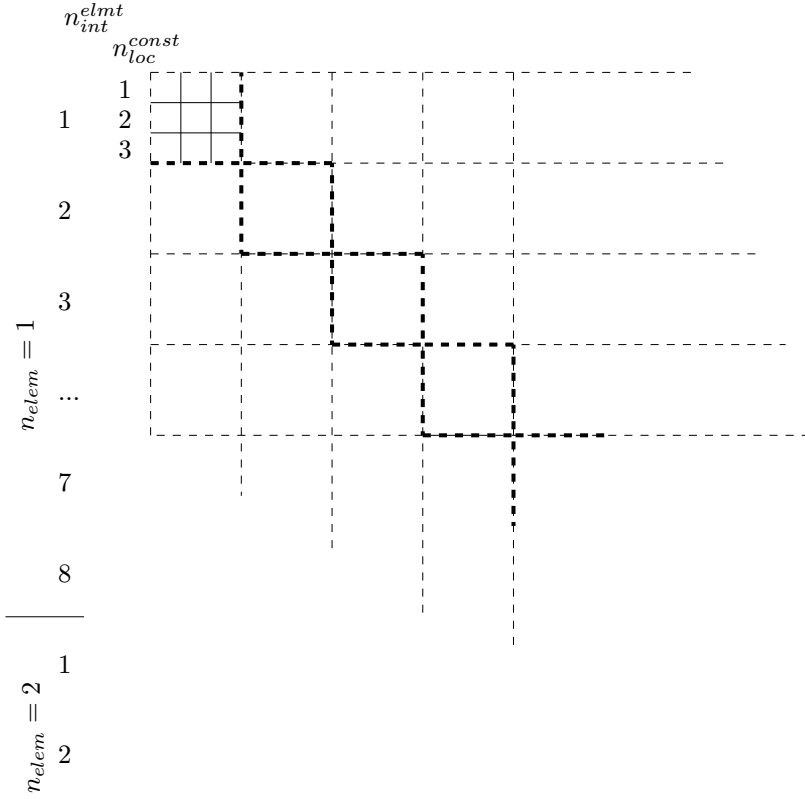


Figure 3.2: Structure of the System Matrix entered by the Constitutive Equations

we need as storage just $(n_{loc}^{const})^2 \cdot n_{int}^{elmt} \cdot n_{elem}$ entries.

Additionally, the iterative character of this solver is the basis for our non-local approach, because after every iteration step we *disturb* the solution for the increment of the damage parameter $\Delta\beta$ by applying the nonlocal BAŽANT-type smoothing (3.1). In this sense, we construct a so-called semi-implicit solution scheme for the set of constitutive equations incorporating the non-local smoothing of the damage parameter. Contrary to the usual strictly explicit computation of (3.1), that procedure can be characterized as advantageous. Writing in matrix notation, we have to solve

$$\mathbf{A} \cdot \mathbf{x} = \mathbf{r} \quad (3.21)$$

for \mathbf{x} as vector of the increments of the constitutive set of equations, where \mathbf{A} is in general nonsymmetric, but stored by the sparse method. An easy

and very efficient method to get a symmetric system of equations, which is required by the LANCZOS solver, applied is to solve the modified system $\mathbf{A}^T \cdot \mathbf{A} \cdot \mathbf{x} = \mathbf{A}^T \cdot \mathbf{r}$. In using iterative equation solvers the efficiency is increased by a *preconditioning* procedure, e.g. see BRAESS [1997]. Here we use a *diagonal* preconditioning, where the preconditioning matrix \mathbf{C} is constructed by the diagonal entries \mathbf{D} of \mathbf{A}^1 :

$$\mathbf{C} = \mathbf{D}_{\mathbf{A}^T \cdot \mathbf{A}} = \mathbf{D}_{\mathbf{A}^T} \cdot \mathbf{D}_{\mathbf{A}} = \mathbf{D}_{\mathbf{A}} \cdot \mathbf{D}_{\mathbf{A}}. \quad (3.22)$$

As consequence we have to solve

$$\mathbf{C}^{-1} \cdot \mathbf{A}^T \cdot \mathbf{A} \cdot \mathbf{x} = \mathbf{C}^{-1} \cdot \mathbf{A}^T \cdot \mathbf{r} \quad (3.23)$$

and during the iteration we have to smooth the solution for $\Delta\beta$ to get the nonlocal results for the increments $\Delta\varepsilon_p$, $\Delta\varepsilon_q$ and $\Delta\beta^{nonloc}$ in every integration point. Having now the *nonlocal* results, the global stiffness and right hand side for the global equilibrium iteration can be assembled following the same scheme as for the classical solution technique.

3.5 Example and Results: Shear band localization

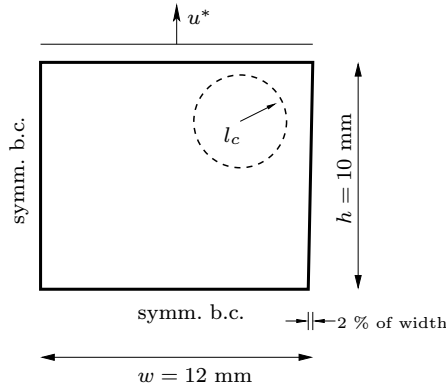


Figure 3.3: One quarter of a stubby plane strain tensile test specimen

¹Notation: $\mathbf{D}_{\mathbf{A}}$ represents the assembling of a matrix \mathbf{D} with $D_{ij} \equiv A_{ij}$ for $i = j$.

E [MPa]	ν	σ_0 [MPa]	N	D	f_0	σ_1 [MPa]
210000	0.3	150	10	3	0.1	400

Table 3.1: Material Parameters

In this article we restrict ourselves to a study of localization of plastic flow in a shear band, using the numerical methods and the 3D finite element formulation described here. The following results could be obtained in an equivalent way by a pure 2D formulation, but here we apply the procedure described above to show that the combination of the ROUSSELIER damage model and the 20-node solid element is able to represent strain localization and ductile failure modes in an efficient way. Further studies have to follow in future. Especially the calibration of this numerical model to experimental data is an important topic of interest. Such examinations are in preparation. We examine the localization in a shear band for a metal strip assuming plain strain conditions. The localization is initiated by a reduced cross-section at the centre of the stubby plane strain tensile test specimen analysed. Due to symmetry just a quarter of the structure is modeled as shown in Fig. 3.3. For that purpose we choose different discretizations characterized by the typical element edge length from $e = 2.0$ mm to $e = 0.25$ mm in the plane of interest. Nevertheless, the model is discretized by the 20-node-solid elements, where plane strain conditions (thickness $t = 0.1$ mm) are enforced. A homogenous displacement u^* is applied at the top of the structure. To force the shear band localization the width of the structure is reduced linearly from the top to the middle (bottom of FE-model) so that the cross-section in the middle of the structure is 2% smaller than that at the top. Additionally, a circle with a radius $r = l_c = 2.0$ mm is drawn in Fig. 3.3 to give an impression of the geometrical proportions relative to the chosen characteristic length scale. The set of material parameters used is shown in Tab. 3.1. For this demonstration of shear band formation no real material behaviour is represented, but reasonable values of the parameters are chosen, such that shear bands form easily and the convergence of the numerical model is stable.

It is noted that there is a “natural margin” for the possible interval of parameters for the ROUSSELIER damage model, restricted by the representation

of the yield condition (3.10). It is seen that

$$\sigma_1 < \frac{\sigma_0}{f_0 D} \quad (3.24)$$

should be valid for the non-loaded, initial elastic regime $\Phi < 0$, which means $p = q = 0$ and $\beta = \varepsilon_{eqv}^{pl} = 0$. Otherwise, the applied predictor-/corrector-procedure described in Sections 3.3.1 and 3.3.2 will not work. Considering a realistic material behaviour for e.g. mild steel this “condition” (3.24) is kept.

First computations are carried out with different element aspect ratios to get an impression of preferred angle for localization in a shear band using the local approach ($l_c \equiv 0$ mm) of the constitutive equations. We vary the number of elements perpendicular to the tensile direction slightly. The reference discretization for the typical element edge length $e = 1.0$ mm is a 12×10 mesh as shown in the middle of Fig. 3.4, and we use one element layer in the thickness direction. This discretization results in an initial element aspect ratio of $r_a = \frac{w}{n_{elmt}} : \frac{h}{10} \equiv 1.0$. We now vary the horizontal number of elements between $n_{elmt} = 6$ and $n_{elmt} = 24$, so that we get the different initial aspect ratios $r_a = 2.0, \dots, 0.5$. For brevity, just the plots for $n_{elmt} = 6$ and $n_{elmt} = 24$ are shown in Fig. 3.4, where the deformed configuration of the finite element mesh and the computated void volume fraction $f = \frac{B(\beta)}{\sigma_1}$ are plotted corresponding to a top displacement of $u^* = 0.6$ mm. It is seen that a shear band develops in all computations from the top left to the right side across the modeled part of the structure. An important result is that the orientation of the shear bands is the same for all different aspect ratios. The shear band develops at an angle of 41° to the horizon, indepedent of the chosen aspect ratio. This result could not be reached by using a *crossed triangle* finite element formulation as also mentioned in MATHUR *et al.* [1994].

No previous investigation of shear band formation according to the ROUSSELIER model has been found, and therefore the critical angle 41° obtained here appears to be a new result. We also note that the different meshes did not affect the critical strain for the onset of localization, which is seen in Fig. 3.5, where the load-displacement-curves for the three cases $n_{elmt} = 6$, $n_{elmt} = 12$ and $n_{elmt} = 24$ are plotted, and agree very well.

It should be emphasized, that this first investigation on the localization behaviour of the chosen element formulation is a computation of exclusively

local character. The number of elements in tensile direction is kept constant, so that no mesh sensitivity is expected for the curves in Fig. 3.5. A mesh sensitivity of the post localization slope will only occur if the element number in the tensile direction is increased so that the band width is reduced relative to the length of the region analysed. Just the angle of localization is the critical aspect of this part of investigation, by which we proof the capability of that element formulation with respect to that point of view.

In contrast, to show the effect of the nonlocal regularization technique introduced here, the *characteristic* length scale is fixed at $l_c = 2.0$ mm. Fig. 3.6 shows the resulting reaction force on the discretized part of the model vs. end displacement for different discretizations in the local formulation, denoted by (1), (2), (3) for meshes with $e = 1$ mm, $e = 0.5$ mm and $e = 0.25$ mm, respectively. As expected, we obtain the well known mesh sensitivity and see: The finer the mesh chosen, the steeper is the negative slope of the load–displacement curve after the onset of localization.

Results are also shown for the nonlocal formulation with $l_c = 2.0$ mm and the above discretizations. Discretizations with $e > l_c$ are not discussed, since in that case the nonlocal formulation will not affect the values in the element integration points essentially. First of all, the local approach here shows the expected mesh sensitivity for the post localization slope, so that relative to curve (1) the negative slope increases for curves (2) and (3). On the other hand, the solutions for the regularized computations, (4), (5) and (6), in Fig. 3.6 show practically no mesh sensitivity for the post localization slope. These three curves remain rather close to curve (1), where the band width is only determined by the rather large element size. Fig. 3.7 shows different deformed configurations of interest for the local and the nonlocal computations, respectively, where the corresponding points for the meshes are marked by dots in Fig. 3.6. As expected, the finest mesh in the local formulation (Fig. 3.7 (b)) represents a much more narrow shear band than that found for the mesh with $e = 1$ mm (Fig. 3.7 (a)). By contrast, the nonlocal results (c) and (d) in the right column of Fig. 3.7 show much weaker indication of the localization. This is caused by the nonlocal smoothing scheme and it shows that the method works. Obviously, one can get an imagination of the shear band size in the representations of Fig. 3.7 by a comparison to the contours of

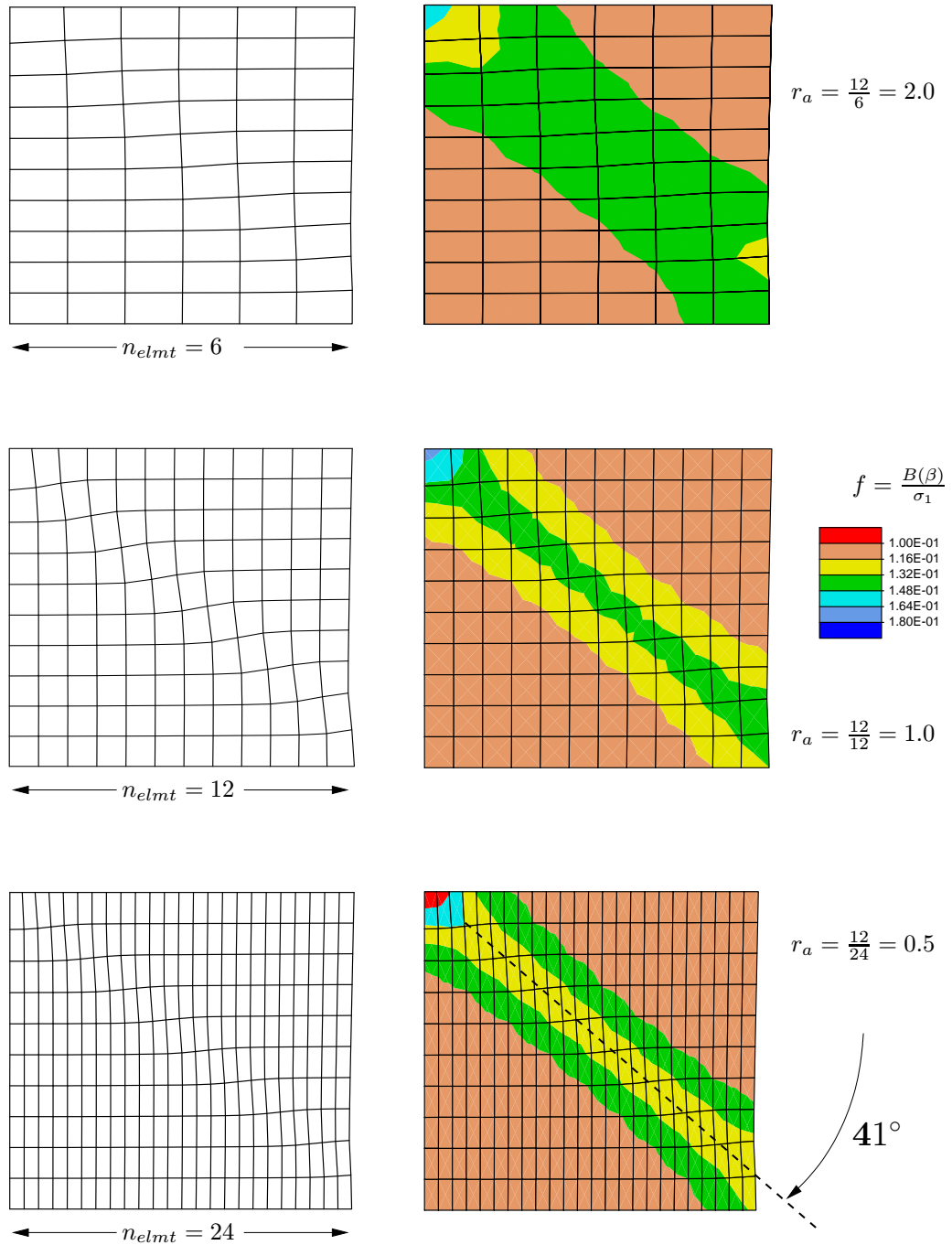
the accumulated plastic strain in Fig. 3.8, where the narrow shear band size of the local approach is visible again. Additionally, we present the identical situation with the contour plots for the accumulated plastic strain ε_{eqv}^{pl} in Fig. 3.8, where the local cases represent again the mesh sensitivity, while on the right hand side the nonlocal results are different because of the spatial smoothing. The left column (Fig. 3.8 a), b)) underlines again the sharp representation of a shear band width of about one element diagonal depending on the respective discretization. If effective strains larger than $\varepsilon_{eqv}^{pl} = 0.06$ are taken to define what is inside the shear band, the shear band widths in Figs. 3.8a, 3.8b, 3.8c and 3.8d are $0.2 \cdot h$, $0.06 \cdot h$, $0.2 \cdot h$ and $0.19 \cdot h$, respectively. This shows, that for the local theory the band width is much reduced in the finer mesh, whereas the nonlocal theory with $l_c = 2$ mm gives approximately equal band width in the two meshes. The obvious appearance of a second shear band above the dominant first one is due to the scaling of the legend. In comparison to Fig. 3.7 b) there is just one shear band activated across the specimen. In contrast the nonlocal results with $l_c = 2$ mm on the right hand side (Fig. 3.8 c), d)) represent the smoothed situations, where the peak values are decreased and the shear band width — especially in Fig. 3.8 d) — is enlarged to the width of Fig. 3.8 c). Again the comparison to Fig. 3.7 d) emphasizes the smeared out appearance of the strain localization in a wider shear band.

3.6 Conclusions

Mesh sensitivity of numerical predictions is avoided here by using a nonlocal damage model, with the delocalization introduced through an integral condition on the increment of the damage quantity. The ROUSSELIER damage model is applied, which describes ductile failure by void growth to coalescence at large plastic strains. A main focus of the paper is the implementation of the nonlocal approach in an iterative NEWTON-RAPHSON scheme, which allows for an accurate numerical solution without the need to use a very large number of small increments. The nonlocal computational model is developed here in the context of a three dimensional finite element formulation, using isoparametric 20-node solid elements, and it is shown that the procedure

works efficiently.

Localization of plastic flow in shear bands is one of the well known examples of strong mesh sensitivity for standard local continuum models, and such behaviour has been investigated for a number of material models. However, predictions of shear band formation due to the softening behaviour in the ROUSSELIER damage model have not been well described. Therefore, the computational examples in the present paper have been used first of all to show the evolution of shear bands under tensile loading, according to the local version of the material model, and to show that the predicted angle of inclination of the shear bands is not mesh sensitive in the present element formulation. Subsequently, the effect of the characteristic material length l_c in the nonlocal formulation is investigated, and it is shown that this removes the mesh sensitivity in the predicted shear band width.

Figure 3.4: Shear Band Localization: *preferred angle* for $l_c = 0$

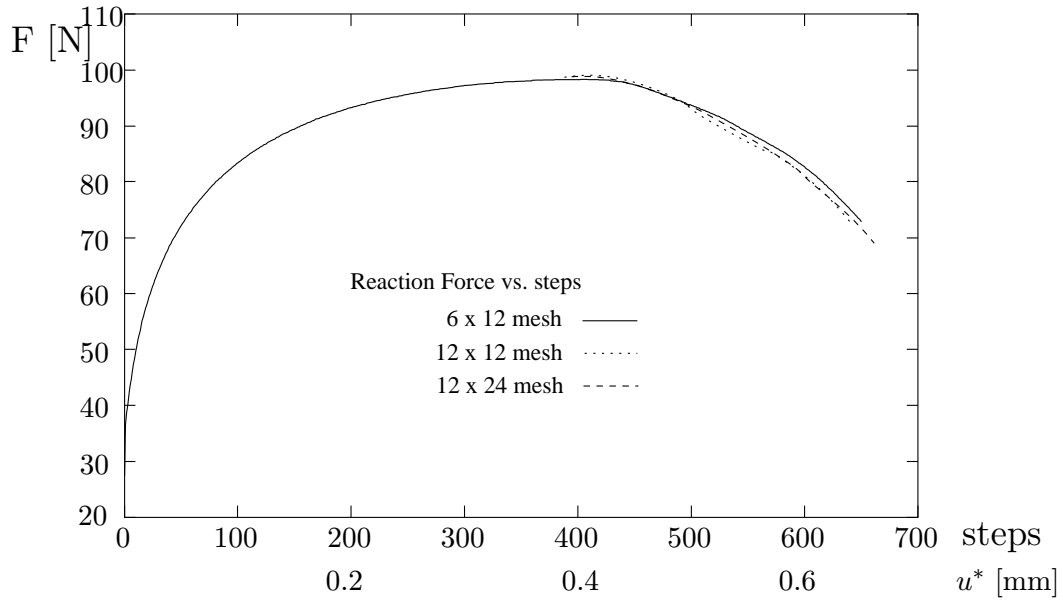


Figure 3.5: Load – displacement for first study: Investigation of preferred angle for different discretizations perpendicular to tensile direction. Local approach ($l_c = 0$), with fixed number of elements in the tensile direction.

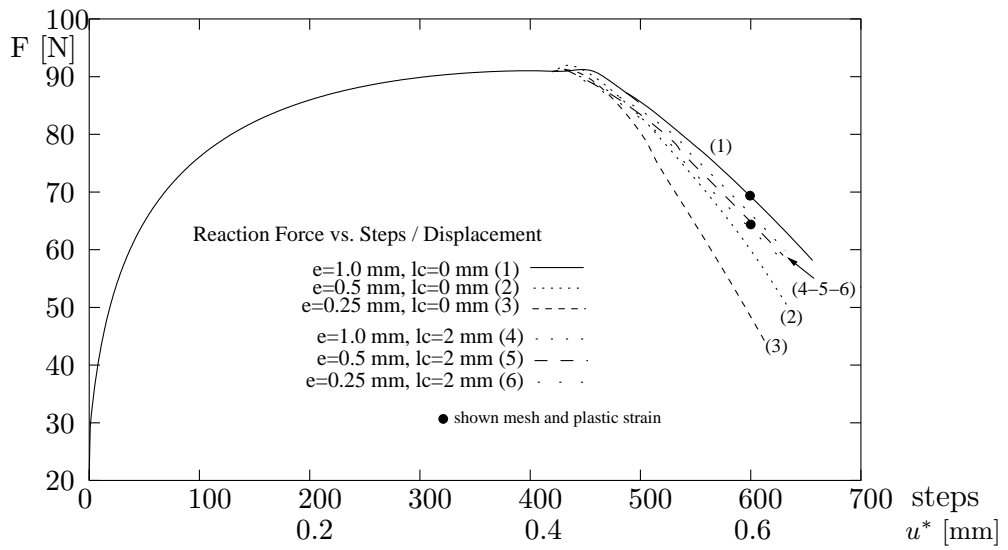


Figure 3.6: Shear Band Localization: Reaction Force vs. End Displacement. Comparison local ($l_c \equiv 0$) – nonlocal ($l_c = 2.0 \text{ mm}$). Discretization increased in both directions, with element size e .

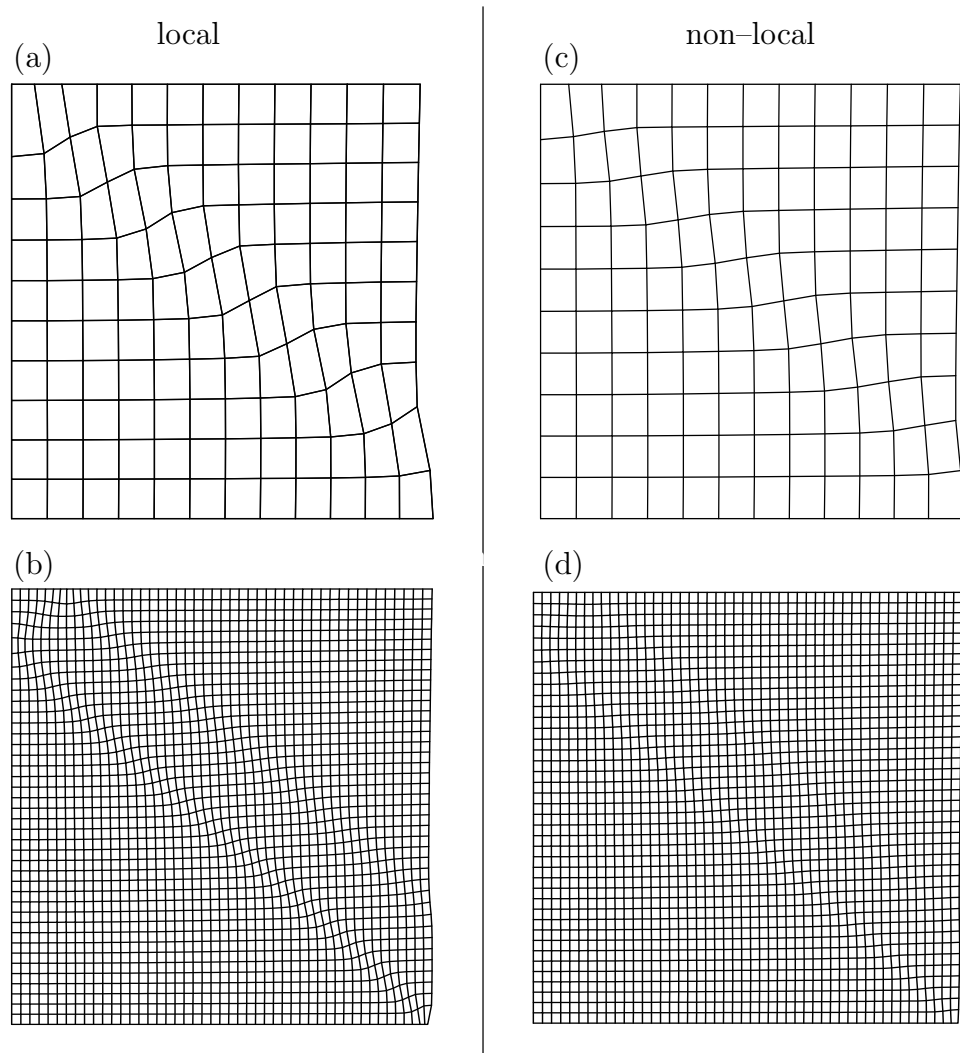


Figure 3.7: Shear Band Localization: Deformed meshes at $u^* = 0.6$ mm. (a) and (c) have $e = 1$ mm; (b) and (d) have $e = 0.25$ mm, where $h = 10$ mm.

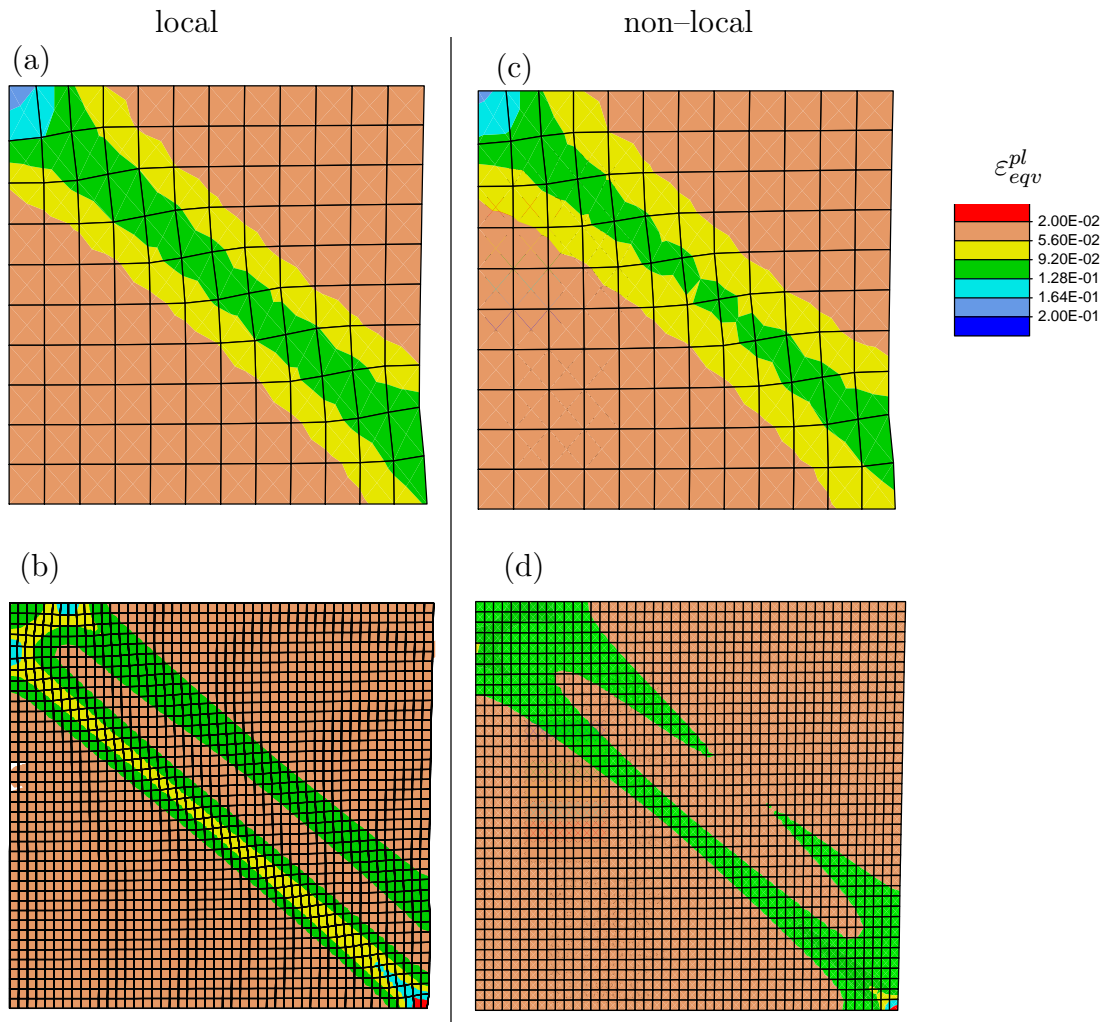


Figure 3.8: Accumulated Plastic Strain at $u^* = 0.6$ mm. (a) and (c) have $e = 1$ mm; (b) and (d) have $e = 0.25$ mm, where $h = 10$ mm.

Appendix

3.7 Iteration of the set of constitutive equations

The unknowns $\Delta\varepsilon_p$, $\Delta\varepsilon_q$ and $\Delta\beta$ are determined by a NEWTON–iteration scheme.

The elastic *trial*–stress state is determined as described in Section 3.3.1, where also the quantities p^{tr} and q^{tr} are obtained as described below (3.8). The “return mapping” iteration described here is carried out for integration points violating the yield condition (3.10), either on the local level or as shown in Sections 3.2.3 and 3.4.2 with the new global algorithm. In both cases the determination of the local JACOBI–matrix is the same.

$$r_1 = \frac{1}{E} \left\{ q - \sigma_0 \left[\frac{\varepsilon_{eq}^{pl}}{\sigma_0} E + 1 \right]^{1/N} + B(\beta) D \exp(-\frac{p}{\sigma_1}) \right\} = \frac{\Phi}{E} = 0 \quad (3.25)$$

$$r_2 = \Delta\varepsilon_p \frac{\partial\Phi}{\partial q} + \Delta\varepsilon_q \frac{\partial\Phi}{\partial p} = 0 \quad (3.26)$$

$$r_3 = \Delta\beta - \Delta\varepsilon_q D \exp(-\frac{p}{\sigma_1}) = 0 \quad (3.27)$$

For having a better *condition* of the iteration system the function r_1 is weighted by YOUNGs modulus, so that a dimensionless expression results as for r_2 and r_3 .

Determination of the JACOBI–matrix as

$$\mathbf{J}^{\text{Rousselier}} = \begin{bmatrix} \frac{\partial r_1}{\partial \Delta\varepsilon_p} & \frac{\partial r_1}{\partial \Delta\varepsilon_q} & \frac{\partial r_1}{\partial \Delta\beta} \\ \frac{\partial r_2}{\partial \Delta\varepsilon_p} & \frac{\partial r_2}{\partial \Delta\varepsilon_q} & \frac{\partial r_2}{\partial \Delta\beta} \\ \frac{\partial r_3}{\partial \Delta\varepsilon_p} & \frac{\partial r_3}{\partial \Delta\varepsilon_q} & \frac{\partial r_3}{\partial \Delta\beta} \end{bmatrix},$$

where the single coefficients are formulated below.

Evaluate for $i, j = 1, 2, 3$

$$\mathbf{x}^{k+1} = \mathbf{x}^k - \Delta\mathbf{x} \quad (3.28)$$

where $\Delta\mathbf{x}$ is either calculated directly on every integration point by $\Delta x_i = J_{ij}^{-1} r_j$ or calculated iteratively using the global LANCZOS- and smoothing scheme by solving $\mathbf{J} \Delta\mathbf{x} = \mathbf{r}$ and adopting (3.1) on $\Delta\beta$.

So one gets $[x_1, x_2, x_3]^T = [\Delta\varepsilon_p, \Delta\varepsilon_q, \Delta\beta]^T$ and update

$$\begin{aligned} p &= p^{tr} + K\Delta\varepsilon_p \\ q &= q^{tr} - 3G\Delta\varepsilon_q \\ \varepsilon_{eqv}^{pl} &= \varepsilon_{eqv}^{pl,tr} + \Delta\varepsilon_q \\ \beta &= \beta^{tr} + \Delta\beta, \end{aligned} \quad (3.29)$$

where K and G are the compression and shear modulus, respectively. The quantities $\varepsilon_{eqv}^{pl,tr}$ and β^{tr} are used to store the accumulated *history* of the actual integration point in addition to the tensoriel quantity needed in (3.7).

The coefficients of $\mathbf{J}^{\text{Rousselier}}$ are determined using the following symbolic manipulations:

$$\begin{aligned} \frac{\partial B}{\partial \beta} &= B(\beta) \frac{1 - f_0}{1 - f_0 + f_0 \exp(\beta)}, & \frac{\partial \sigma^*}{\partial \varepsilon_{eqv}^{pl}} &= \frac{E}{N} \left[\frac{\varepsilon_{eqv}^{pl}}{\sigma_0} E + 1 \right]^{1/N-1} \\ \frac{\partial \Phi}{\partial p} &= -B(\beta) \frac{D}{\sigma_1} \exp(-\frac{p}{\sigma_1}), & \frac{\partial \Phi}{\partial q} &= 1 \\ \frac{\partial \Phi}{\partial \beta} &= \frac{\partial B}{\partial \beta} D \exp(-\frac{p}{\sigma_1}), & \frac{\partial^2 \Phi}{\partial p \partial \beta} &= -\frac{\partial B}{\partial \beta} \frac{D}{\sigma_1} \exp(-\frac{p}{\sigma_1}) = -\frac{1}{\sigma_1} \frac{\partial \Phi}{\partial \beta} \end{aligned} \quad (3.30)$$

$\frac{\partial r_1}{\partial \Delta\varepsilon_p} = \frac{\partial \Phi}{\partial p} \frac{K}{E}$	$\frac{\partial r_1}{\partial \Delta\varepsilon_q} = \frac{1}{E} (-3G - \frac{\partial \sigma^*}{\partial \varepsilon_{eqv}^{pl}})$	$\frac{\partial r_1}{\partial \Delta\beta} = \frac{1}{E} \frac{\partial \Phi}{\partial \beta}$
$\frac{\partial r_2}{\partial \Delta\varepsilon_p} = 1 - \Delta\varepsilon_q \frac{\partial \Phi}{\partial p} \frac{K}{\sigma_1}$	$\frac{\partial r_2}{\partial \Delta\varepsilon_q} = \frac{\partial \Phi}{\partial p}$	$\frac{\partial r_2}{\partial \Delta\beta} = \Delta\varepsilon_q \frac{\partial^2 \Phi}{\partial p \partial \beta}$
$\frac{\partial r_3}{\partial \Delta\varepsilon_p} = \Delta\varepsilon_q D \frac{K}{\sigma_1} \exp(-\frac{p}{\sigma_1})$	$\frac{\partial r_3}{\partial \Delta\varepsilon_q} = -D \exp(-\frac{p}{\sigma_1})$	$\frac{\partial r_3}{\partial \Delta\beta} = 1$

3.8 The preconditioned LANCZOS solver algorithm solving $\mathbf{K} \cdot \mathbf{x} = \mathbf{r}$

1. Initialization	
(a)	start with RHS
(b)	\mathbf{r} with $\mathbf{x}_0 = \mathbf{0}$
(c)	preconditioning
(d)	$\mathbf{q} = \mathbf{0}, \mathbf{c} = \mathbf{0}, d = 0, \delta = 0$
(e)	$\mathbf{z} = \mathbf{C}^{-1}\mathbf{r}$
	$\beta = \sqrt{\mathbf{r}^T \mathbf{z}}$
	$\bar{\mathbf{q}} = \mathbf{z}/\beta$
2. Iteration, till $RES < TOL$	
(a)	$\mathbf{z} = \mathbf{K}\bar{\mathbf{q}}$
(b)	$\alpha = \bar{\mathbf{q}}^T \mathbf{z}$
(c)	diagonals
(d)	$d = \alpha - \delta^2 d_{old}$
	$\zeta = \begin{cases} \beta/d & \text{on 1st loop} \\ -\delta \zeta_{old} d_{old}/d & \text{else} \end{cases}$
(e)	$\mathbf{c} = \bar{\mathbf{q}} - \delta \mathbf{c}_{old}$
(f)	$\mathbf{x} = \mathbf{x}_{old} + \zeta \mathbf{c}$
(g)	new LANCZOS–vector
(h)	$\mathbf{q} = \mathbf{r}/\beta$
(i)	$\mathbf{r} = \mathbf{z} - \alpha \mathbf{q} - \beta \mathbf{q}_{old}$
(j)	$\mathbf{z} = \mathbf{C}^{-1}\mathbf{r}$
(k)	$\beta = \sqrt{\mathbf{r}^T \mathbf{z}}$
(l)	$\bar{\mathbf{q}} = \mathbf{z}/\beta$
(m)	$RES = \beta \zeta $

Kapitel 4

**Remarks on the Use of
Continuum Damage Models
and on the Limitations of their
Applicability in Ductile
Fracture Mechanics**

**in: *Deformation and Failure in
Metallic and Granular Materials***

**LECTURE NOTES IN APPLIED AND
COMPUTATIONAL MECHANICS**

**eds. K. Hutter and H. Baaser,
Springer, 2003**

Remarks on the Use of Continuum Damage Models and on the Limitations of their Applicability in Ductile Fracture Mechanics

HERBERT BAASER and DIETMAR GROSS

*Institute of Mechanics, Darmstadt University of Technology
Hochschulstr. 1, D-64289 Darmstadt, Germany
[{baaser, gross}@mechanik.tu-darmstadt.de](mailto:{baaser,gross}@mechanik.tu-darmstadt.de)*

received 23 Aug 2002 — accepted 29 Oct 2002

Abstract: Ductile crack initiation and growth is investigated by applying a three-dimensional finite element analysis in conjunction with a nonlinear damage model. This numerical procedure is formally restricted by the so-called *loss of ellipticity* due to a type change of the differential equations. A time-independent finite strain formulation is applied, based on a multiplicative decomposition of the deformation gradient in an elastic and a plastic part leading to an efficient integration scheme. This formulation can be used as a general interface for the implementation of different constitutive models describing damage by a scalar quantity in an isotropic manner. As examples, we show some details of the thermomechanics of the ROUSSELIER and the GURSON damage models.

We discuss the description of microscopically strongly inhomogeneous material behaviour by discretization methods using macroscopic mechanical field quantities, which are microscopic averages. Often, typical discretization length scales fall below the intrinsic material length scales, making the averaging structure of the applied numerical method doubtful. We present a detailed analysis of their limitations and a comparative study of the investigated damage models for the simulation of ductile fracture problems.

4.1 Introduction

During the past years application of models based on continuum damage mechanics (CDM) to ductile fracture mechanics became very popular.

The computational evaluation and simulation of damage occurrence by different models implemented in the framework of the finite element method (FEM) seems to be very promising, since many contributions have followed the first, fundamental publications such as GURSON [1977], ROUSSELIER *et al.* [1989], TVERGAARD [1989]. It is commonly believed that application of the FEM taking finite deformations into account in conjunction with advanced constitutive damage models with a softening regime may be capable of simulating crack initiation and growth in typical fracture specimens under test conditions. A well-known disadvantage of the numerical treatment of solid mechanics problems, where softening material behaviour occurs, is the so-called *mesh-dependence* of numerical results. In a considerable number of investigations different methods have been proposed to overcome this mesh-dependence. The common idea is to introduce a *characteristic* or *internal* length (scale) into the constitutive model or its evaluation, see BAASER & GROSS [1998], BAASER & GROSS [2001a], BAASER & TVERGAARD [2003] and references therein, where a summary of different regularization techniques is outlined.

In this paper some limitations and restrictions of the ductile damage mechanics analysis are pointed out in the scope of the finite element method and its nonlinear solution procedures at the example of a so-called COMPACT TENSION (CT) specimen . In order to resolve the highly nonlinear effects of stress and strain concentration occurring near notches, crack tips or due to shear band localization, the numerical discretization in these regions usually is refined without respecting minimal length scales limited by *inhomogeneities* on the microscale of the material. Typical physically based length scales of ductile materials such as structural steel or aluminium alloys are in the magnitude of about $50\mu\text{m} - 200\mu\text{m}$. However, very often, length scales resulting from FE discretizations of detailed simulations of damage and crack initiation and growth problems fall below these “natural” barriers. As a consequence, the basic assumptions of continuum mechanics such as continuity of mechanical quantities on the macroscale are definitely violated and the numerical results are highly questionable.

In this study, 20-noded brick elements are used with quadratic shape functions along the element edges. As constitutive models, the ductile damage

models of ROUSSELIER *et al.* ROUSSELIER *et al.* [1989] and GURSON GURSON [1977] in the formulation of TVERGAARD TVERGAARD [1989] are used in the scope of isotropic finite strain plasticity. An advantage of the first model is the description of material softening due to damage by the influence of solely three material parameters, while the GURSON model incorporates essentially a larger parameter set sometimes leading to non-definite solutions, see ZHANG & HAUGE [1999]. A second advantage of the ROUSSELIER model is related to the numerical implementation of the constitutive law by means of an implicit integration scheme. The type of constitutive equations leads to symmetric tangent material moduli, which is advantageous in computing and storing the matrix expressions. To this end, we will remark for both models on internal variables and their thermomechanical relations with respect to the dissipation inequality.

Simultaneously, a localization analysis is performed during the iteration on each integration point by evaluation of the so called *localization* or *acoustic tensor* for all possible directions of localization in three dimensions. The fundamental derivation of the acoustic tensor for finite strains is described in STEINMANN *et al.* [1997]. An essential result of localization analysis for damage occurrence in a CT specimen under monotonic loading is the fact that a detailed representation of the behaviour of local strain softening is possible obviously beyond the peak load, but is restricted as long as no loss of ellipticity occurs.

4.2 Three-dimensional Finite Element Formulation

Starting point of any finite element discretization is the weak form of equilibrium, given here in a spatial description as

$$g(\mathbf{u}, \delta\mathbf{u}) := \int_{\mathcal{B}} \boldsymbol{\sigma} \operatorname{grad} \delta\mathbf{u} \, dv - \int_{\partial\mathcal{B}_\sigma} \mathbf{t}_L \delta\mathbf{u} \, da = 0, \quad (4.1)$$

where $\mathbf{u} = \mathbf{x} - \mathbf{X}$ denotes the displacement vector of a material point represented by \mathbf{X} in the reference configuration toward a position \mathbf{x} of the same point in the current configuration, $\delta\mathbf{u}$ is the first variation of the displacement field. With $\boldsymbol{\sigma}$ the CAUCHY stress tensor is characterized and $\mathbf{t}_L = \boldsymbol{\sigma} \cdot \mathcal{N}$ are the prescribed tractions acting on the loaded boundary $\partial\mathcal{B}_\sigma$ of the body with (outer) normal vector \mathcal{N} in the current configuration \mathcal{B} .

Linearization at a known position $\mathbf{X} + \hat{\mathbf{u}}$ with respect to the current deformation state and rearrangement leads to the following representation of the element stiffness

$$\Delta g^{elmt}(\hat{\mathbf{u}}, \delta\mathbf{u}) = \int_{\mathcal{B}} (\Delta\boldsymbol{\sigma} + \text{grad}\Delta\mathbf{u} \cdot \boldsymbol{\sigma}) : \text{grad } \delta\mathbf{u} \, dv^{elmt}, \quad (4.2)$$

where $\Delta(\bullet)$ denotes the linearization operator and $\Delta\mathbf{u} = \mathbf{u} - \hat{\mathbf{u}}$ the increment of the displacement field \mathbf{u} . The right part of (4.2) results in the element stiffness *matrix* \mathbf{K}^{elmt} for the discretized setting, where \mathbf{K}^{elmt} obviously consists of two parts. The first part is obtained from the consistent linearization of the material model getting $\Delta\boldsymbol{\sigma}$ and the second part comes solely from the linearization of the used strain measure at the computed stress state $\boldsymbol{\sigma}$. For further details on the implementation of the consistent linearization of the used algorithm see SIMO [1992]. The discretization chosen in this paper is

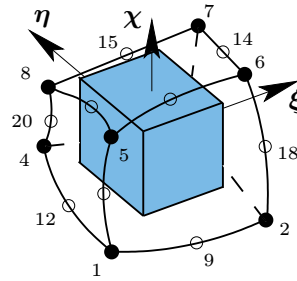


Figure 4.1: 20–node–displacement element with corner nodes • and edge nodes ○

based on a 20-node-displacement element formulation with shape functions N_i , ($i = 1, 2, \dots, 20$), so that quadratic functions describe the element edges. As in MATHUR *et al.* [1994], a $2 \times 2 \times 2$ integration scheme is used, which

means an *underintegration* with respect to the quadratic shape functions N_i . It shall be pointed out that no *hourgassing* modes were detected as for an 8-node–displacement element formulation and a $1 \times 1 \times 1$ integration scheme, see BAASER & GROSS [1998].

4.3 Treatment of Continuum Damage Models in the Scope of Isotropic Finite Strain Plasticity

4.3.1 Continuum Damage Models

Following ARAVAS [1987] we write the KIRCHHOFF stress tensor $\boldsymbol{\tau}$ as the weighted CAUCHY stress tensor as

$$\boldsymbol{\tau} = J \boldsymbol{\sigma} = -p^\tau \mathbf{I} + 2/3 q^\tau \hat{\mathbf{n}} , \quad (4.3)$$

where $J := \det \mathbf{F}$ is the determinant of the deformation gradient $\mathbf{F} = \partial \mathbf{x} / \partial \mathbf{X}$ mapping material points \mathbf{X} onto the current configuration \mathbf{x} . The scalar $p^\tau = -\tau_{ij} \delta_{ij} / 3$ defines the hydrostatic pressure, $q^\tau = \sqrt{3/2 t_{ij} t_{ij}}$ is the equivalent KIRCHHOFF stress and $t_{ij} = \tau_{ij} + p^\tau \delta_{ij}$ are the components of the KIRCHHOFF stress deviator. These quantities can also be obtained for the CAUCHY stress tensor, whose deviatoric stress is $\mathbf{s} = \boldsymbol{\sigma} + p^\sigma \mathbf{I}$. In this notation, an additional important quantity is the normalized and dimensionless stress deviator

$$\hat{\mathbf{n}} = 3/(2q^\tau) \mathbf{t} = 3/(2q^\sigma) \mathbf{s} . \quad (4.4)$$

The second order unit tensor \mathbf{I} is defined as the KRONECKER symbol by its components δ_{ij} in the cartesian frame. Analogous, the plastic strain rate can be written as

$$\Delta \boldsymbol{\epsilon}^p = \frac{1}{3} \Delta \varepsilon_p \mathbf{I} + \Delta \varepsilon_q \hat{\mathbf{n}} , \quad (4.5)$$

where $\Delta \varepsilon_p$ and $\Delta \varepsilon_q$ describe scalar rate quantities which are defined below. Note, that again the dimensionless tensor quantities \mathbf{I} and $\hat{\mathbf{n}}$ are used in this notation.

The first constitutive model used in this study is the damage model proposed by ROUSSELIER *et al.* ROUSSELIER *et al.* [1989]. Here, taking ductile damage processes into account, the yield function is written as

$$\Phi^{Rouss} = q^\tau - \underbrace{\sigma_0 \left[\frac{\varepsilon_{eqv}^p}{\sigma_0} E + 1 \right]^{1/N}}_{\sigma_M} + B(\beta) D \exp(-\frac{p^\tau}{\sigma_1}) = 0, \quad (4.6)$$

where σ_M represents the material hardening in terms of a power law, and the last part of (4.6) describes the damage (softening) behaviour through the function $B(\beta)$ and an exponential expression. Furthermore, E is the YOUNG modulus, σ_0 is the initial yield stress, N is the material hardening exponent, and D and σ_1 are *damage* material parameters. The function $B(\beta)$ is the *conjugate force* to the damage quantity β , defined by

$$B(\beta) = \frac{\sigma_1 f_0 \exp(\beta)}{1 - f_0 + f_0 \exp(\beta)}. \quad (4.7)$$

Here, the initial void volume fraction f_0 is the third damage-depending material parameter used in this constitutive set of equations. The evolution equation for the damage parameter β is given by $\Delta\beta = \Delta\varepsilon_q D \exp(-p^\tau/\sigma_1)$, which is obviously dependent on the deviatoric part of the strain rate $\Delta\varepsilon_q$ and the actual hydrostatic pressure p^τ .

In the following some details of the constitutive model are pointed out:

1. The current value of the void volume fraction f can be determined by $f = B(\beta)/\sigma_1$. This quantity enables a comparison with other damage models, like TVERGAARD [1989].
2. The yield function (4.6) can be regarded as the classical yield condition of the VON MISES plasticity with the hardening function $\sigma^*(\varepsilon_{eqv}^{pl})$ expanded by a third term responsible for the material softening.
3. Note that for a vanishing initial void volume fraction $f_0 \equiv 0$ the yield condition (4.6) indicates a VON MISES yield condition without any influence of damage. However, in that case no increase of the damage quantity β will take place. This is in contrast to common formulations of GURSON's damage model, where especially a nucleation of microvoids

is taken into account by an extra term in addition to the evolution equation of the void volume fraction f , see TVERGAARD [1989]. The constitutive formulation used here describes “damage” by the parameter β , which has no direct correlation to a measurable quantity. In so far no specific term for the nucleation of microvoids is assumed. With $f_0 \equiv 0$ there will be no influence of the evolution equation $\Delta\beta$ on $B(\beta)$ and (4.6). Furthermore, the algebraic reformulation of (4.12) will break down because of the vanishing derivative $\partial\Phi/\partial p$ in (4.12)₁. In view of such a numerically based argumentation it is necessary to define at least a small initial void volume fraction f_0 in order to get an evolution of the damage parameter β .

4. Considering the HELMHOLTZ free energy

$$\Psi(\mathbf{b}_e, \varepsilon_{eqv}^{pl}, \beta) = W(\mathbf{b}_e) + H_1(\varepsilon_{eqv}^{pl}) + H_2(\beta), \quad (4.8)$$

which can additively be split into the elastic part W and the parts H_1 and H_2 connected to the internal variables ε_{eqv}^{pl} and β ; the conjugate forces $q = -\partial H_1/\partial \varepsilon_{eqv}^{pl}$ and $B(\beta) = -\partial H_2/\partial \beta$ can be identified via differentiation. Alternatively, one can obtain the “damage potential”

$$H_2 = - \int_{\beta_0}^{\beta} B(\bar{\beta}) d\bar{\beta} = B_0 - [\sigma_1 \ln(1 - f_0 + f_0 \exp(\beta))] \quad (4.9)$$

from an explicit integration of (4.7), with $B_0 = \sigma_1 \ln(1 - f_0 + f_0 \exp(\beta_0))$ as additional material parameter depending on the initial damage state¹. The relation (4.9) is graphically depicted in Fig. 4.2, where the shaded area represents the dissipated “damage work” for a considered interval $[0, \beta]$. This is in contrast to the following GURSON model, where such a potential cannot be found, see STEINMANN *et al.* [1994].

¹Nach einer Anmerkung von Prof. Tsakmakis ist diese Modifikation mit β_0 bzw. B_0 hier im Zuge der Habilitation in Abweichung zum ursprünglichen Artikel eingefügt worden. Damit ist gewährleistet, dass über alle möglichen Deformationsprozesse $H_2 > 0$ bleibt, was thermodynamisch zwingend ist, vgl. (4.8). In Erweiterung zu ROUSSELIER *et al.* [1989] wird diese Anforderung für das hier verwendete Schädigungsmodell auch erst in ROUSSELIER [2001] diskutiert !

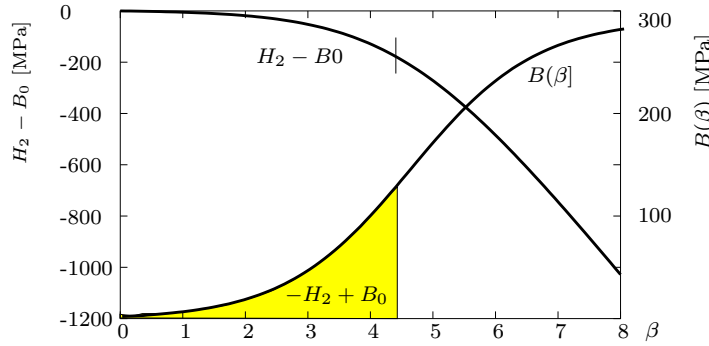


Figure 4.2: Damage potential $H_2 - B_0$ for the ROUSSELIER model and *damage force* $B(\beta)$ vs. damage parameter β (parameter $\sigma_1 = 300$ MPa, $f_0 = 0.01$ from Table 4.2)

The second constitutive model adopted here is the damage model of GURSON in the formulation of TVERGAARD [1989], the numerical treatment follows BAASER & GROSS [2000]. In contrast to (4.6) the yield function appears in a slightly different form as

$$\Phi^{Gurson} = \left(\frac{q^\sigma}{\sigma_M} \right)^2 + 3f^*(f) \cosh\left(-\frac{3}{2} \frac{p^\sigma}{\sigma_M}\right) - \left[1 + \left(\frac{3}{2} f^*(f)\right)^2 \right] = 0 , \quad (4.10)$$

while the numerical treatment is identical for both models. In order to enable a comparison with the ROUSSELIER model, we assume an evolution of void volume fraction f solely by growth of existing voids and neglect the term describing void nucleation. The hardening of the matrix material is again described by σ_M and the actual void volume fraction f enters the yield function (4.10) as f^* , where $f^*(f)$ is defined by a bilinear function following TVERGAARD [1989].

The macroscopic plastic strain rate $\dot{\epsilon}^p$ is determined by the classical associated flow rule

$$\dot{\epsilon}^p = \gamma \frac{\partial \Phi}{\partial \boldsymbol{\tau}} = \gamma \left\{ \frac{\partial \Phi}{\partial q^\tau} \frac{\partial q^\tau}{\partial \boldsymbol{\tau}} + \frac{\partial \Phi}{\partial p^\tau} \frac{\partial p^\tau}{\partial \boldsymbol{\tau}} \right\} \quad (4.11)$$

with the plastic multiplier γ . Note that $\dot{\epsilon}^p$ coincides with the plastic increment $\Delta\epsilon^p$ for the algorithmic setting written in principal axes and is identified as the plastic part of the spatial deformation velocity tensor \mathbf{d} in the finite strain

regime later on. The bracket on the right-hand side of (4.11) shows a further advantage of this formulation following ARAVAS [1987], since it is easy to determine the derivatives of Φ with respect to the scalar quantities q^τ and p . It can be seen with (4.11) that

$$\Delta\varepsilon_p = -\gamma \frac{\partial\Phi}{\partial p^\tau} \quad \text{and} \quad \Delta\varepsilon_q = \gamma \frac{\partial\Phi}{\partial q^\tau}. \quad (4.12)$$

These two equations allow the algebraic elimination of the factor γ . Thus, the increment of the plastic strain can be expressed by the two scalar quantities $\Delta\varepsilon_p$ and $\Delta\varepsilon_q$. Furthermore, the equivalent plastic strain ε_{eqv}^p can be incremented directly by $\Delta\varepsilon_q$.

With this, the set of constitutive equations is completed. The evaluation of the material model on the local level of integration points for a given load is realized by an implicit EULER backward integration scheme for the unknowns $\Delta\varepsilon_p$, $\Delta\varepsilon_q$ and $\Delta\beta$. The exact linearization of the set of equations follows the description in ARAVAS [1987]. The variational expression

$$\delta\boldsymbol{\tau} = \mathbb{C}_e : \left(\delta\boldsymbol{\epsilon}^{tr} - \frac{1}{3}\delta\Delta\varepsilon_p \mathbf{I} - \delta\Delta\varepsilon_q \hat{\mathbf{n}} - \Delta\varepsilon_q \frac{\partial\hat{\mathbf{n}}}{\partial\boldsymbol{\tau}} : \delta\boldsymbol{\tau} \right) = \mathbb{D}_{Algo}^{\text{Material}} : \delta\mathbf{e} \quad (4.13)$$

leads, after some extended algebraic manipulations as described in ARAVAS [1987], to the expressions $\delta\Delta\varepsilon_p$ and $\delta\Delta\varepsilon_q$, where \mathbb{C}_e characterizes the elastic material modulus. Finally, we obtain the algorithmic material modulus $\mathbb{D}_{Algo}^{\text{Material}}$ at the end of the considered time interval $[t, t + \Delta t]$, which is necessary to compute the complete stiffness in (4.2). Note, that the consistent linearization of the algorithmic modulus in (4.13) leads to a unconditionally symmetric matrix representation for the ROUSSELIER model, and to a symmetric representation for the GURSON model just for neglecting void nucleation as treated here.

4.3.2 Finite Strain Plasticity

At least in the crack tip region of elastic–plastic solids under sufficiently high load, finite deformations occur where the plastic part of the strains usually is large compared with the elastic part. The framework of multiplicative elastoplasticity is used. Its kinematic key assumption is the multiplicative

split of the deformation gradient

$$\mathbf{F} = \mathbf{F}_e \cdot \mathbf{F}_p \quad (4.14)$$

into an elastic and a plastic part, providing the basis of a geometrically exact theory and avoiding linearization of any measure of deformation. Note that

$$d\hat{\mathbf{x}} = \mathbf{F}_p \cdot d\mathbf{X} = \mathbf{F}_e^{-1} \cdot d\mathbf{x} \quad (4.15)$$

introduces a so-called *intermediate configuration*, which quantities are labeled by $(\hat{\bullet})$. As a further advantage, fast and numerically stable iterative algorithms, proposed and described in SIMO [1992], can be used. In the following, only a brief summary of the integration algorithm for a time step $[t_n; t_{n+1}]$ in the context of a FE-implementation is given. Note that in the following the index $n + 1$ is suppressed for brevity if misunderstanding is unlikely to occur.

The essential aspect of the multiplicative decomposition is the resulting additive structure of the current logarithmic principal strains within the return mapping scheme as $\boldsymbol{\epsilon}^e = \boldsymbol{\epsilon}^{tr} - \Delta\boldsymbol{\epsilon}^p$. Here, $\boldsymbol{\epsilon}^e$ and $\boldsymbol{\epsilon}^{tr}$ stand for a vector representation with the components $\epsilon_i^e = \ln \mu_i^e$ and $\epsilon_i^{tr} = \ln \mu_i^{tr}$, respectively, strictly connected with the spectral decomposition of the elastic left CAUCHY–GREEN tensor.

The elastic left CAUCHY–GREEN tensor can be specified with the multiplicative decomposition as

$$\mathbf{b}_e = \mathbf{F}_e \cdot \mathbf{F}_e^T = \mathbf{F} \cdot \mathbf{C}_p^{-1} \cdot \mathbf{F}^T, \quad (4.16)$$

where the superscripts “-1” and “T” denote the inverse and the transpose of a tensor, respectively. That relation clearly shows the “connection” between the elastic and plastic deformation measure by the occurrence of the plastic right CAUCHY–GREEN tensor $\mathbf{C}_p = \mathbf{F}_p^T \cdot \mathbf{F}_p$. By means of the relative deformation gradient, see SIMO [1992],

$$\mathbf{f} = \partial \mathbf{x}_{n+1} / \partial \mathbf{x}_n = \mathbf{F}_{n+1} \cdot \mathbf{F}_n^{-1}, \quad (4.17)$$

which relates the current configuration \mathbf{x}_{n+1} to the configuration belonging to the previous time step at t_n , an elastic *trial*–state $\mathbf{b}_e^{tr} = \mathbf{f} \cdot \mathbf{b}_n \cdot \mathbf{f}^T$ is calculated for the current configuration with frozen internal variables at state t_n .

In the considered case of isotropy, \mathbf{b}_e commutes with $\boldsymbol{\tau}$, see REESE & WRIGGERS [1997], SIMO [1992]. We assume to fix the principle axes of \mathbf{b}_e during the return mapping scheme described in the previous section, so that the spectral decomposition

$$\mathbf{b}_e^{tr} = \sum_{i=1}^3 \mu_i^{tr 2} \mathbf{n}_i^{tr} \otimes \mathbf{n}_i^{tr} \quad (4.18)$$

is given and the eigenvectors \mathbf{n}_i^{tr} can also be used to compose the stress tensor $\boldsymbol{\tau} = \sum_{i=1}^3 \tau_i \mathbf{n}_i^{tr} \otimes \mathbf{n}_i^{tr}$. That motivates the evaluation of the constitutive equations given in the previous section in principle axes, which means additionally a time saving compared to an evaluation of all six (symmetric) tensor components.

Furthermore, for the elastic part of the material description compressible Neo-Hooke behaviour is used, where the plastic strain corrector $\Delta\epsilon^p$ is obtained by the normality rule of plastic flow (4.11).

The general concept of LIE time derivative $\mathcal{L}_{\mathbf{v}}(\bullet)$ characterizing the change of a spatial field in the direction of the vector \mathbf{v} and known to yield objective spatial fields, see HOLZAPFEL [2000], leads in this case to the OLDROYD rate of the elastic left CAUCHY–GREEN tensor

$$\mathcal{L}_{\mathbf{v}} \mathbf{b}_e = \overset{\nabla}{\mathbf{b}}_e = \dot{\mathbf{b}}_e - \mathbf{l} \cdot \mathbf{b}_e - \mathbf{b}_e \cdot \mathbf{l}^T \quad (4.19)$$

where $\dot{\mathbf{b}}_e$ denotes the material time derivative and $\mathbf{l} = \text{grad } \dot{\mathbf{x}} = \dot{\mathbf{F}} \cdot \mathbf{F}^{-1}$ the spatial velocity gradient. In this case \mathbf{v} is identified as velocity vector $\mathbf{v} = \dot{\mathbf{x}} = \partial \mathbf{x} / \partial t$. The decomposition of $\mathbf{l} = \mathbf{d} + \mathbf{w}$ in its symmetric part $\mathbf{d} = \text{sym}(\mathbf{l}) = \frac{1}{2}(\mathbf{l} + \mathbf{l}^T)$ and its antimetric part \mathbf{w} , known as spin tensor, respectively, plays a crucial role in the definition of the plastic flow rule. Some basic algebraic manipulations let us also obtain the expressions in (4.19) as

$$\mathcal{L}_{\mathbf{v}} \mathbf{b}_e = -2 \mathbf{F}_e \cdot \text{sym}(\hat{\mathbf{l}}_p) \cdot \mathbf{F}_e^T = -2 \text{sym}(\mathbf{l}_p \cdot \mathbf{b}_e) , \quad (4.20)$$

where $\hat{\mathbf{l}}_p$ is defined by $\hat{\mathbf{l}}_p = \dot{\mathbf{F}}_p \cdot \mathbf{F}_p^{-1}$ acting on the intermediate configuration. Please note, that we do *not* make any assumption concerning the antimetric part \mathbf{w} of \mathbf{l} . Because of the restriction to isotropic material behaviour, the focus is just directed to the symmetric part \mathbf{d} of \mathbf{l} . So, the additive decomposition $\mathbf{d} = \mathbf{d}_e + \mathbf{d}_p$ results from the multiplicative decomposition $\mathbf{F} = \mathbf{F}_e \cdot \mathbf{F}_p$.

The definition of the associated flow rule (see also (4.11)) in that finite strain regime as

$$\mathbf{d}_p := \gamma \frac{\partial \Phi}{\partial \boldsymbol{\tau}} \quad (4.21)$$

enables with (4.19) and (4.20) the formulation

$$\mathcal{L}_{\mathbf{v}} \mathbf{b}_e = -2 \operatorname{sym}(\gamma \frac{\partial \Phi}{\partial \boldsymbol{\tau}} \cdot \mathbf{b}_e) . \quad (4.22)$$

If the condition $\Phi \leq 0$ (see (4.6) and (4.10)) is fulfilled by the current stress state $\boldsymbol{\tau}$, this state is possible and it is the solution. If, on the other hand, $\Phi \leq 0$ is violated by the trial-state, the trial stresses must be projected back on the yield surface $\Phi = 0$ in an additional step, often called “exponential return mapping”.

In that case, $\mathbf{x} = \mathbf{x}_{n+1}$ is fixed and (4.22) results in

$$\overset{\triangledown}{\mathbf{b}}_e = \dot{\mathbf{b}}_e = -2\gamma \operatorname{sym}(\frac{\partial \Phi}{\partial \boldsymbol{\tau}} \cdot \mathbf{b}_e) , \quad (4.23)$$

with $\mathbf{l} \equiv \mathbf{0}$. The solution of the first order differential equation (4.23) is given by

$$\mathbf{b}_{e n+1} = \sum_{i=1}^3 \underbrace{\exp [2\epsilon_i^e]}_{\mu_i^{e2}} \mathbf{n}_{i n+1}^{tr} \otimes \mathbf{n}_{i n+1}^{tr} , \quad (4.24)$$

where the elastic logarithmic strains ϵ^e are obtained in principle axes, see (4.11–4.12), so that $\mathbf{b}_{e n+1}$ is known and $\mathbf{C}_p^{-1} = \mathbf{F}^{-1} \cdot \mathbf{b}_{e n+1} \cdot \mathbf{F}^{-T}$ can be stored as *history variable* for the next time step.

4.4 Localization Analysis

4.4.1 Acoustic Tensor

A steady evaluation of the “spatial localization tensor” \mathbf{Q} is performed on each integration point during the iteration to check the material stability. The spatial localization tensor $\mathbf{Q} = \mathbf{n} \cdot \mathbb{D} \cdot \mathbf{n}$ is the contraction of the current fourth order material tensor \mathbb{D} by the spatial surface unit normal vector

\mathbf{n} with respect to its second and fourth index. This derivation, introduced in STEINMANN *et al.* [1997], is motivated by the assumption of a spatially continuous incremental equilibrium across an arbitrary band of discontinuity, which implies that the nominal traction rate inside and outside the band is the same:

$$\overset{\circ}{\mathbf{t}}(\mathbf{x}^{out}) = \overset{\circ}{\mathbf{t}}(\mathbf{x}^{band}) . \quad (4.25)$$

With the definition of the nominal traction rate $\overset{\circ}{\mathbf{t}} = J^{-1}\overset{\circ}{\boldsymbol{\tau}} \cdot \mathbf{n}$, the nominal rate of the KIRCHHOFF stress tensor $\overset{\circ}{\boldsymbol{\tau}}$ can be related to the spatial velocity gradient $\mathbf{l} := \dot{\mathbf{F}} \cdot \mathbf{F}^{-1}$ via

$$\overset{\circ}{\boldsymbol{\tau}} = \overset{\circ}{\mathbb{D}} : \mathbf{l} . \quad (4.26)$$

Note that the material tensor splits off into $\overset{\circ}{\mathbb{D}} = \overset{\circ}{\mathbb{D}}^{Material} + \overset{\circ}{\mathbb{D}}^{Geometry}$, where the first part results from the linearization of the constitutive equations and the second part is obtained by the linearization of the geometrical setting. This is in strong equivalence to the formulation of the element stiffness matrix for the discretized representation of (4.2) in Sec. 4.2. A detailed discussion is given in PETRYK [1997]. These relations become more evident by reformulation of the material rate of the first PIOLA–KIRCHHOFF stress tensor $\dot{\mathbf{P}}$ in terms of the KIRCHHOFF stress tensor $\boldsymbol{\tau}$ into

$$\dot{\mathbf{P}} = \mathbf{F}^{-1} \cdot \dot{\boldsymbol{\tau}} - \mathbf{F}^{-1} \cdot \mathbf{l} \cdot \boldsymbol{\tau} . \quad (4.27)$$

Relating $\dot{\mathbf{P}}$ to the rate of the deformation gradient, $\dot{\mathbf{F}}$, via the tangent map $\overset{\circ}{\mathbb{D}}^P$ yields

$$\overset{\circ}{\boldsymbol{\tau}} = \dot{\boldsymbol{\tau}} - \mathbf{l} \cdot \boldsymbol{\tau} = \mathbf{F} \cdot \overset{\circ}{\mathbb{D}}^P : \dot{\mathbf{F}} , \quad (4.28)$$

which is related to the known *frame-invariant (objective)* OLDROYD rate $\overset{\nabla}{\boldsymbol{\tau}}$ by $\overset{\circ}{\boldsymbol{\tau}} = \overset{\nabla}{\boldsymbol{\tau}} + \boldsymbol{\tau} \cdot \mathbf{l}^T$. Note that the derivations and argumentation in SCHREYER & NEILSEN [1996] about the loss of material stability by real or imaginary wave speeds very illustratively denote the term “acoustic tensor”. The double contraction $\mathbf{Q} = \mathbf{n} \cdot \overset{\circ}{\mathbb{D}} \cdot \mathbf{n}$ of the material tensor $\overset{\circ}{\mathbb{D}}$ by the normal vector \mathbf{n} indicates a possible wave propagation direction. By this the normal of a possible failure plane is characterized. The condition for obtaining well set numerical results is the positive definiteness of the second order tensor \mathbf{Q} , which is checked by a positive value of the determinant $q = \det[\mathbf{Q}]$.

4.4.2 Numerical treatment

In the numerical analysis $q = \det[\mathbf{Q}] = \det[\mathbf{n} \cdot \mathbb{D} \cdot \mathbf{n}]$ has to be evaluated for all possible directions \mathbf{n} at every location \mathbf{x} . For that reason the vector $\mathbf{n} = [\cos \lambda \cos \varphi, \sin \lambda \cos \varphi, \sin \varphi]^T$ is parameterized by spherical coordinates with the angles λ and φ characterizing the longitude and the latitude, respectively. Note, that — as a simplification — we use the algorithmic material tensor $\mathbb{D}_{Alg}^{\text{Material}}$ as part of \mathbb{D} , knowing that both, $\mathbb{D}^{\text{Material}}$ and $\mathbb{D}_{Alg}^{\text{Material}}$, differ from one another for sufficiently large time steps. This difference should be subjected to further investigations.

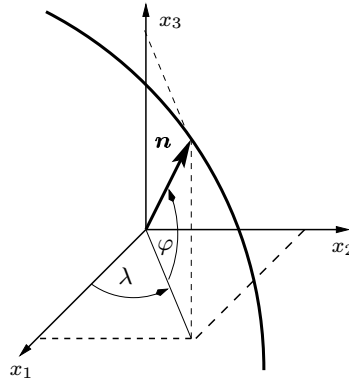


Figure 4.3: Parametrization of \mathbf{n} with longitude angle λ and latitude angle φ

To detect a possible critical direction, where q may vanish, one has to compute $q = \det[\mathbf{Q}] \rightarrow \min$ for a set $\{\lambda, \varphi\}$. As a remark, it should be mentioned here, that for the general 3D case q is a function of terms in the power of six, e.g. $\sin^6 \lambda$ or $\cos^6 \varphi$. This minimization procedure is equivalent to the evaluation of $\nabla q(\lambda, \varphi) = \mathbf{0}$, for which we propose a classical NEWTON iteration scheme through

$$\begin{bmatrix} \lambda \\ \varphi \end{bmatrix}_{k+1} = \begin{bmatrix} \lambda \\ \varphi \end{bmatrix}_k - \underbrace{\begin{bmatrix} \frac{\partial^2 q}{\partial \lambda^2} & \frac{\partial^2 q}{\partial \lambda \partial \varphi} \\ \frac{\partial^2 q}{\partial \lambda \partial \varphi} & \frac{\partial^2 q}{\partial \varphi^2} \end{bmatrix}}_{=: \mathbf{H}^{-1}}^{-1} \cdot \begin{bmatrix} \frac{\partial q}{\partial \lambda} \\ \frac{\partial q}{\partial \varphi} \end{bmatrix}, \quad (4.29)$$

and suitable initial conditions, e.g. $[\lambda, \varphi]_0^T = [10^\circ, 80^\circ]_0^T$, where k indicates the iteration loop number. Note, that the choice of the initial conditions is of specific interest for solving this problem and is still in discussion, see ORTIZ *et al.* [1987] or WELLS & SLUYS [2001].

Because of the large number of operations needed especially for determining the HESSE matrix \mathbf{H} in (4.29), the expressions of the related FORTRAN code are obtained by the algebraic manipulation program MATHEMATICA exploiting some advanced methods for code generation. Still, in this case (3D, $\mathbb{D}^{\text{Material}}$ symmetric) evaluation of more than 6100 multiplications for determining *one* of the inverse of the HESSE matrix \mathbf{H} during the iteration loop in the integration points would be necessary, which is comparable to the inversion of a 35×35 -matrix by GAUSS elimination. By sophisticated substitutions of different terms in q it is possible to reduce the maximum exponent from 6 to 2, which is much more accessible for compiler optimization procedures. Furthermore, the total number of multiplications is reduced to about 670, so that the amount of compiling \mathbf{H} is minimized.

4.5 Example and Results

4.5.1 Model of a CT specimen

As an example, a three-dimensional model of a CT specimen discretized by 20-node solid elements as shown in Fig. 4.4(a) is examined. Due to symmetry, just a quarter of the structure is modeled, for length dimensions see Table 4.1. The loading is applied by a prescribed displacement u_F (by 0.01 mm/step) of the nodes lying on the marked line, see Fig. 4.4(a). The chosen discretization is characterized by the typical element edge length e in front of the crack tip. In this investigation the element edge lengths $e = 0.50$ mm and $e = 0.25$ mm are used. In addition, the typical mesh sensitive results for a classical, local FE simulation using different discretizations are plotted as load-deflection curve in Fig. 4.4(b). The dependence of the reaction force on the finite element mesh can clearly be seen. The set of geometry and material

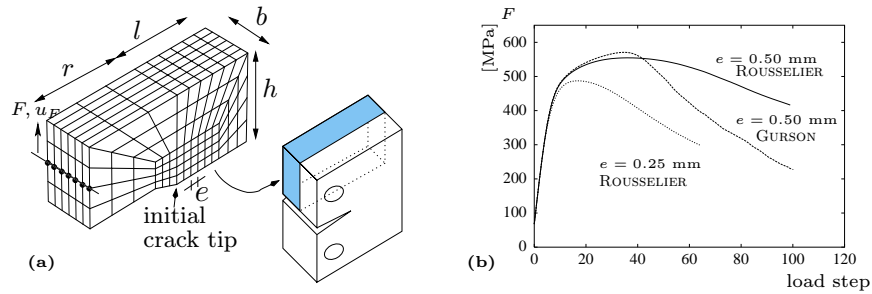


Figure 4.4: (a) Model of CT specimen and (b) typical load–deflection curve for different discretizations

Table 4.1: Geometry and (hardening) material parameters

r [mm]	l [mm]	b [mm]	h [mm]	E [MPa]	ν	σ_0 [MPa]	N
6	5	3	5	210000	0.2	460	7

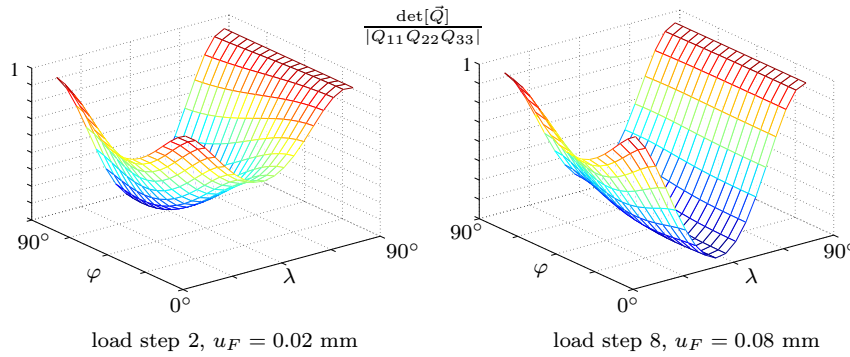
parameters used is shown in Table 4.1, where the four parameters describing the elastic and hardening behaviour can be obtained by simple tensile tests. The parameters of Table 4.2 are responsible for the damage representation of the constitutive models. For this contribution we fitted the parameter f_c of the GURSON model to the fixed set of parameters used for the ROUSSELIER damage description by trying to obtain sufficient agreement between the global load–deflection curves in Fig. 4.4(b) for both models using e.g. $e = 0.5 \text{ mm}$. The parameter f_F representing the final void volume fraction of the GURSON model does not effect the respective load–deflection curves in the first part, where no crack advance occurs.

4.5.2 Results

A result for the load–displacement curves for different discretizations is plotted in Fig. 4.4(b) and can also be found in BAASER & GROSS [2001a]. The

Table 4.2: Damage material parameters for both models

<i>both</i>	ROUSSELIER		GURSON	
f_0	D	σ_1 [MPa]	f_c	f_F
0.01	3	300	0.008	0.19

Figure 4.5: Decrease of $q = \det [\mathbf{Q}]$ for $u_F = 0.02$ mm and $u_F = 0.08$ mm

mesh sensitivity is obvious, if no additional regularization technique is applied. In the following, we concentrate on computations resulting from the evaluation of the localization tensor \mathbf{Q} and its determinant. The representation of the results is focused on the FE-integration point being located directly in front of the crack tip in the center of the specimen, which is the point with the largest load and the highest damage parameter. Figure 4.5 shows the normalized determinant of \mathbf{Q} vs. the two spatial angles λ and φ , parameterizing the normal vector \mathbf{n} in each case by 20 steps (ROUSSELIER parameter set of Table 4.1 and $e = 0.50$ mm). Displayed is the situation for load steps 2 and 8 ($u_F = 0.02, 0.08$ mm), which represents directly the situation before the onset of localization ($q \rightarrow 0$). Obviously, the decrease of $q/|Q_{11}Q_{22}Q_{33}|$ during load steps 2 to 8 can be seen.

Because of the numerical costs determining these quantities during the iteration, we apply a NEWTON iteration scheme following (4.29) for finding the minimum of these surfaces. For the mentioned integration point, Fig. 4.6(a) shows $\det [\mathbf{Q}]$ vs. 30 load steps for two different discretizations with

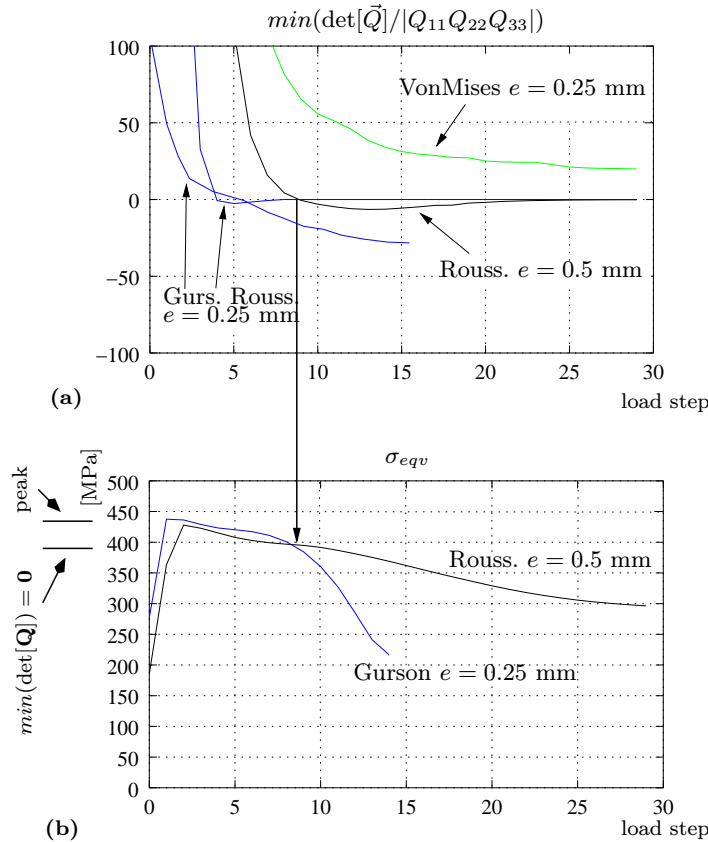


Figure 4.6: (a) Determinant of acoustic tensor \mathbf{Q} and (b) equivalent stress in front of the crack tip. Difference between *peak* load and level of zero crossing is marked at the vertical axis of (b)

$e = 0.50 \text{ mm}$ and $e = 0.25 \text{ mm}$ and ROUSSELIER material, respectively. In addition, the situation for a standard (non damaging) VON MISES material with the same power-hardening law σ^* and $e = 0.50 \text{ mm}$ is plotted. As expected, for the VON MISES material, the values of q decrease rapidly during the load incrementation over 30 steps, but never reach $q = 0$ indicating a possible localization. In contrast, the curves for the ROUSSELIER damage material show a zero-crossing and thus a localization occurrence. Again, the mesh sensitivity is obvious through the results for $e = 0.25 \text{ mm}$ at load step 4, while the discretization with $e = 0.50 \text{ mm}$ reaches zero at load level 9.

In Fig. 4.6(b) the equivalent stress of the integration point in front of the

crack tip is plotted vs. the applied load steps for the ROUSSELIER material and $e = 0.50$ mm. Note that the equivalent stress at the critical load level 9 ($u_F = 0.09$ mm) appears in the decreasing part of the load curve obviously after reaching the peak load.

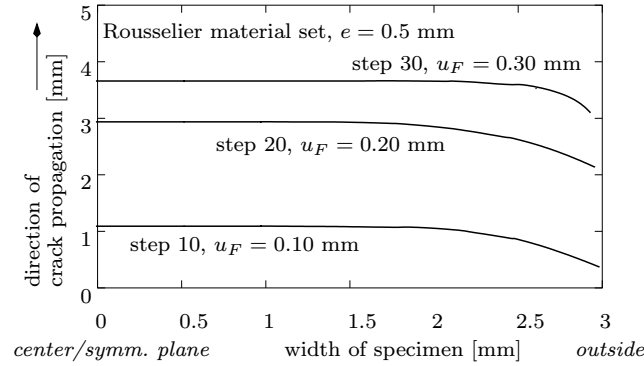


Figure 4.7: Contours of integration points on the ligament reaching $q = 0$ for load steps 10, 20, 30 using the ROUSSELIER material set and $e = 0.50$ mm

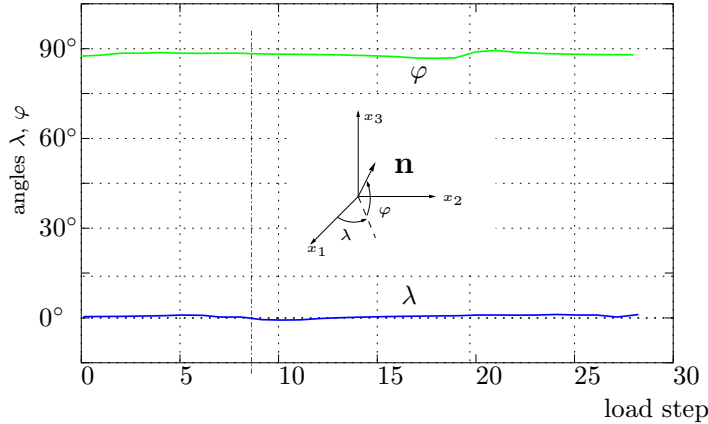


Figure 4.8: Orientation of \mathbf{n} in front of the crack tip. The vertical line marks the load step of loosing ellipticity for the considered problem, cf. Fig. 4.6

In Fig. 4.7 the contours of integration points are depicted, where the determinant of the acoustic tensor reaches zero for the load steps 10, 20 and 30 in front of the crack tip. The contour lines in crack propagation direction are plotted over the discretized width b of the specimen using $e = 0.50$ mm

and the ROUSSELIER material set of Table 4.1 demonstrating local loss of ellipticity in front of the crack tip during the computation. It should be emphasized, that the contour lines $q = 0$ do not coincide with the contour lines of lost load carrying capacity (crack growth) defined by a critical damage parameter. These crack growth contours follow the $q = 0$ contours far behind (at higher load steps), indicating that they are determined in inadmissible situations.

In Fig. 4.8 the angles λ and φ characterizing the normal \mathbf{n} of the failure plane of the highest loaded integration point in front of the crack tip are plotted. Obviously, the computations show nearly constant results $\lambda = 0^\circ$ and $\varphi = 90^\circ$, which describes the classical *mode I* failure regime for the considered CT specimen.

The results show impressingly the close limits of the continuum damage mechanics using the FE method without additional regularization avoiding a type change of the leading differential equation. Mesh refinements resulting in the typical mesh sizes in the magnitude of the intrinsic material length scales can not represent the real, potentially inhomogeneous, material structure on the microlevel.

4.6 Summary

In this contribution we present a study on ductile damage analysis by a 3D simulation of CT specimen using the ROUSSELIER damage model within a finite element formulation based on 20-node–solid elements. The main attention was focused on the limitations of the finite element method discretizing mechanical field equations by piecewise continuous functions, which are used to represent inhomogeneous constituents of material on the microscale.

Typical FE analyses, resolving the situations in front of crack tips or in shear band regions as detailed as possible, are known to produce mesh sensitive results because of the changing type of the basic differential equations. This “loss of ellipticity” is checked by a steady evaluation of the acoustic tensor and a stop of the overall computation reaching such a point of stability.

It is worth mentioning that this critical situation is reached early during the nonlinear iteration process, so that the subsequently determined numerical results become questionable, if no method of regularization is applied.

Kapitel 5

**Analysis of void growth in a
ductile material in front of a
crack tip**

**COMPUTATIONAL MATERIAL
SCIENCE, 26(C): 28–35, 2003**

Analysis of void growth in a ductile material in front of a crack tip

H. BAASER, D. GROSS

Institute of Mechanics, Darmstadt University of Technology, D-64289 Darmstadt
baaser@mechanik.tu-darmstadt.de

Abstract: *The growth of microvoids in a ductile material is analysed in front of a crack tip loaded by a remote K_I -field. For this purpose, a circular region with radius R around the crack tip containing statistically distributed initially circular microvoids of radii r is discretised. The material behaviour is described by classical J_2 -plasticity with power hardening law in the scope of finite deformations. The process region is subdivided into a patch of randomly generated polygons simulating a real crystallic microstructure with a characteristic length scale. Within these polygons the material behaviour is represented by the identical, above mentioned assumptions and constitutive model but with a statistical deviation from their average values. The second part focuses on the representation of geometrically necessary dislocations (GND) in the context of the applied finite strain description within the FE formulation. The aim of this investigation is a deeper understanding of correlations between material and geometrical properties of mode I dominated ductile damage and failure processes. Results of the parameter studies show strain distributions around typical microvoids and along the ligament.*

Keywords: Ductile Damage, Void Growth, Geometrically Necessary Dislocations (GND), VORONOI-tessellation

PACS: 62.20F, 61.50.C, 61.72, 61.72.Q

5.1 Introduction

The aim of this study is a detailed computational analysis of the growth of microvoids in a ductile material in front of a crack tip loaded by a remote

K_I -field. Damage and failure analysis in ductile metallic materials due to microvoid growth has been subjected to intensive research activities in the past decades. While the models of the *continuum damage approach* are extended in a steady development, see PARDOEN & HUTCHINSON [2000], and many contributions treat with multi-level computations applying different homogenization techniques for micro-macro transitions, see MIEHE *et al.* [1999] or GHOSH *et al.* [2001], an increasing number of investigations deal with micro-structure computations exclusively on the level of the materials crystalline or grain structure. On this micro-scale of investigation, many known phenomena of macroscopic material behaviour can reasonably be studied and explained. Objects of interest are e.g. grain boundary sliding, see VAN DER GIJSEN & TVERGAARD [1994], or dislocation behaviour, see ORTIZ *et al.* [2000], which have an essential influence on damage and failure due to several mechanisms of void growth. Such substructure investigations introduce an additional length scale by defining the geometry (shape, diameter etc.) of the particles building up the microstructure. The first investigations of discrete voids in front of a crack tip assume a homogenized material behaviour in the domain of interest, see ARAVAS & McMEEKING [1985], while some newer contributions study micro-structure behaviour in samples with periodic arrangements of hexagonal cells, see VAN DER GIJSEN & TVERGAARD [1994] or MIEHE *et al.* [1999]. Further studies deal with randomly distributed voids and analyse differences of crack propagation in there, AL-OSTAZ & JASIUK [1997]. A statistical continuum theory applied to the microstructure of polycrystalline material is given for the case of large plastic deformation by GARMESTANI *et al.* [2001].

A post-processing procedure for the investigation of the evolution of *geometrically necessary dislocations* (GND) is described. GND evolution occurs during plastic deformation processes due to the *incompatible* character of the plastic part of the deformation gradient $\mathbf{F}^p = \mathbf{F}^{e-1} \cdot \mathbf{F}$, which is not necessarily the gradient of a vector field. This topic is the object of many contributions since the works of KONDO [1952] and BILBY *et al.* [1955] in the early 1950's and e.g. KRÖNER [1958] dealing with the representation of dislocations in the context of differential geometry. A precise review of these developments is given by DE WIT [1981].

The success in computational mechanics during the last 10–15 years in the treatment of a generalized and unified description of material behaviour based on a multiplicative decomposition of the deformation gradient (see e.g. WEBER & ANAND [1990] or SIMO [1992]) focuses — in quite a natural way — on suitable representations of the *internal constraints* due to the incompatibility of \mathbf{F}^e and \mathbf{F}^p . Recent contributions deal with this correlations, see STEINMANN [1996] and CERMELLI & GURTIN [2001].

For the purpose of this study, a circular region with radius R around the crack tip containing statistically distributed initially circular microvoids of radii r is discretised by 6-noded triangular finite elements under plane strain conditions. The global load is realized by prescribed displacements, representing a K_I -dominated far field. The material behaviour is described by classical J_2 -plasticity with a power hardening law introducing the initial yield stress σ_0 and the hardening exponent N in the scope of finite deformations. The process region is subdivided into a patch of randomly generated polygons simulating a *real* crystallic microstructure with the characteristic length scale L , so that $r \ll L \ll R$. Within these polygons, the material behaviour again is represented by the identical, above mentioned assumptions and constitutive model but with a statistical deviation from their average values. In order to represent a crystallographic texture, this seems to be an easy and effective method to describe microscopic *inhomogeneity* resulting in a macroscopically anisotropic behaviour. But it should be clearly stated, that these first assumptions are not able to capture the effects of plastic anisotropy. Further investigations considering mechanisms of crystal plasticity have to follow in this context.

Having in mind the simulation of a microstructure as realistic as possible, where the size of grains in typical steel or aluminium applications reaches from about $200\text{ }\mu\text{m}$ down to about 3 to $5\text{ }\mu\text{m}$, we investigate, in this contribution, the more or less fine-grained spectrum of metals of interest by choosing two typical average grain sizes of $L \simeq 8\text{ }\mu\text{m}$ and $L \simeq 19\text{ }\mu\text{m}$. Obviously, the length scales of this investigation are directly coupled with those of *real metallic material* and emphasize the fact, that the length scales of metallic damage and failure processes, which are often assumed to take place in a so called *process zone*, are of the same order. Due to these statements

a representation of metallic damage and failure occurrence by constitutive models of *continuum damage mechanics* becomes very questionable, because the material behaviour e.g. near crack tip singularities is still not understood enough and the basic assumptions of *continuum theory* as *continuity of displacement fields* and *homogeneity in the surrounding of a material point \mathbf{x}* are violated in these regions.

The aim of this investigation is a deeper understanding of basic correlations between material and geometrical properties in the situation of mode I dominated ductile damage and failure processes. Results of the parameter studies and the detailed FE calculations show strain and stress distributions around typical microvoids and along the ligament. In addition, the void growth is shown by illustrative plots of the deformed microstructure and void shapes. These representations suggest certain failure modes and seem to be very revealing with respect to a dependence of the intrinsic length scales.

5.2 Computational Treatment

5.2.1 Generation of Heterogeneous, Crystalline Microstructure

This two-dimensional computational investigation is carried out in a circular K_I -dominated remote field with radius $R = 2$ mm and a crack tip positioned in the origin under plane strain conditions. In the surrounding of the crack tip, a window of approximately $50 \times 50 \mu\text{m}$ edge length is modeled with a randomly generated crystalline-like substructure, as can be seen in Fig. 5.1. During the computation the validity of small-scale-yielding is checked by the size of the plastic zone. The evolution of plastic strain is still observed to concentrate in the modeled process zone, so that the small-scale-yielding conditions can be assumed as not violated. For this contribution, we use two different substructures. The first with about 100 (here $L \simeq 19 \mu\text{m}$) and the second with about 300 ($L \simeq 8 \mu\text{m}$) subdomains, each of them represents a single crystallite. These subdomains within the window of interest around the crack tip are generated by a random determination of the node points and a following DELAUNAY-triangulation including its dual VORONOI-diagram.

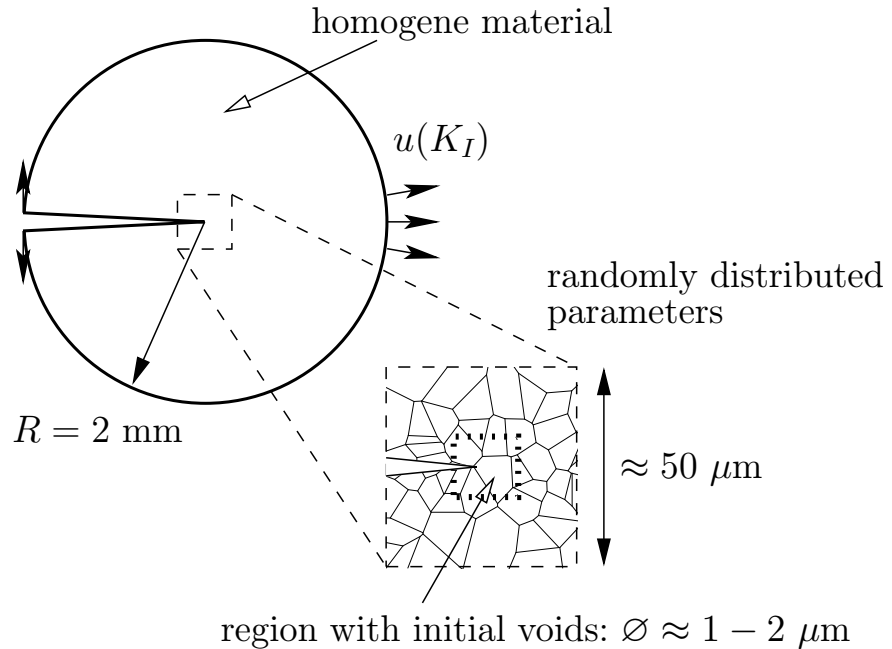


Figure 5.1: K_I loaded domain. Zoomed out crack tip region.

See SHEWCHUK [1996] for the partly used generation code **Triangle**, which is extended by a special postprocessor for the determination of coherent regions of a single crystallite. Assuming ideal conditions for crystal growth, the generated structure can be seen as a synthetic texture representation by grains grown from randomly distributed nucleation, start growing at the same time with constant and equal growing velocity.

Within this region containing a grain-like substructure, exemplary eleven microvoids are positioned randomly with different initial radius r near the crack tip, see Fig. 5.2. The positions and the radii of the assumed microvoids are listed in Tab. 5.1. That geometrical arrangement of the voids is used for the both modeled substructures as can be seen in Fig. 5.2. The resulting regions in this way are discretized by the classical 6-noded triangular finite elements, whose constitutive behaviour is assigned to a set of material parameters deviating from average values. In contrast, the constitutive behaviour of the encompassing circular region is modeled by classical J_2 plasticity theory for large strains but homogeneous parameter distribution of averaged values $\bar{\sigma}_0$ and

\bar{N} .

5.2.2 FEM–Formulation and Constitutive Behaviour

In elastic-plastic solids under sufficiently high load finite deformations occur, where the plastic part of the strains usually is large compared to the elastic part. We use the framework of multiplicative elastoplasticity. Its kinematic key assumption is the multiplicative split of the deformation gradient

$$\mathbf{F} = \mathbf{F}^e \cdot \mathbf{F}^p \quad (5.1)$$

into an elastic and a plastic part, providing the basis of a geometrically exact theory and avoiding linearization of any measure of deformation. As a further advantage, fast and numerically stable iterative algorithms, proposed and described in WEBER & ANAND [1990], can be used. If the condition

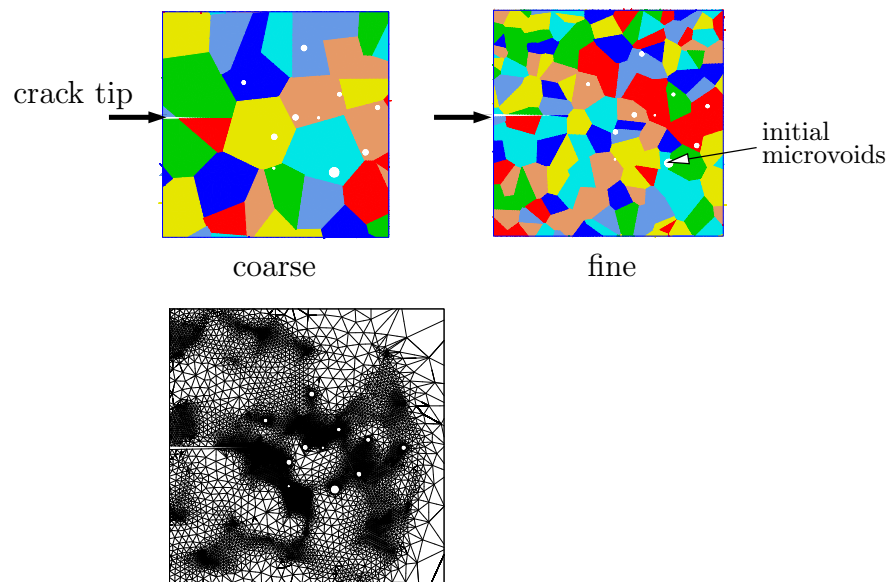


Figure 5.2: Crack tip region with same initial void distribution, but different microstructure. Discretization for coarse mesh.

$\Phi \leq 0$ (see eqn. (5.2)) is fulfilled by the current stress state $\boldsymbol{\tau}$, this state is possible and is the solution. If, on the other hand, $\Phi \leq 0$ is violated by the trial-state, the trial stresses must be projected back on the yield

#void	1	2	3	4	5	6
<i>xpos</i>	12.55	18.25	7.3	23.4	44.3	-0.25
<i>ypos</i>	0.1	0.0	-4.7	5.85	0.0	8.75
<i>radius</i>	1.0	0.6	1.0	0.8	0.9	0.8
#void	7	8	9	10	11	
<i>xpos</i>	29.85	14.65	22.1	7.2	32.85	
<i>ypos</i>	-8.55	17.3	-13.5	-12.45	2.55	
<i>radius</i>	1.0	1.0	1.5	0.6	0.85	

Table 5.1: Position and radius of randomly distributed microvoids; length dimension [μm]

surface $\Phi = 0$ in an additional step. This return mapping procedure is used as the integration algorithm for the constitutive equations described below. It should be mentioned that the algorithmic treatment in terms of principal axes has some advantages concerning computational aspects like time and memory saving. The constitutive model used in this study is a classical J_2 flow theory. Here, the yield function is written as

$$\Phi = q - \sigma_0 \left[\frac{\varepsilon_{eqv}^{pl}}{\sigma_0} E + 1 \right]^{1/N} = 0, \quad (5.2)$$

where $q = \sqrt{\frac{3}{2}t_{ij}t_{ij}}$ is the equivalent KIRCHHOFF stress, $p = -\frac{1}{3}\tau_{ij}\delta_{ij}$ defines the hydrostatic pressure, and $t_{ij} = \tau_{ij} + p\delta_{ij}$ are the components of the KIRCHHOFF stress deviator. Furthermore, YOUNGS modulus is defined by E , the initial yield stress by σ_0 and the material hardening by the exponent N . The set of constitutive equations is complemented by the evolution equations for the plastic strain. The macroscopic plastic strain rate $\dot{\epsilon}^{pl}$ is determined by the classical associated flow rule $\dot{\epsilon}^{pl} = \lambda \partial\Phi/\partial\boldsymbol{\tau}$, whereas the parameter λ is determined through the consistency condition $\lambda \dot{\Phi} = 0$ during any plastic flow process.

5.2.3 Applied Loading

The boundary nodes of the discretized structure positioned at radius R are loaded by the displacement field

$$\begin{pmatrix} u_x \\ u_y \end{pmatrix} = \frac{K_I}{2G} \sqrt{\frac{R}{2\pi}} (3 - 4\nu - \cos \varphi) \begin{pmatrix} \cos \varphi/2 \\ \sin \varphi/2 \end{pmatrix}, \quad (5.3)$$

as given in polar coordinates R, φ due to the K_I far field for plane strain conditions, see Fig. 5.1. So the stress intensity factor K_I determines the amplitude of the crack tip field, G represents the shear modulus and ν the POISSON number. For this contribution K_I is initially set to $K_I^{ref} = 10 \text{ MPa}\sqrt{\text{m}}$ and is incremented stepwise linearly with slope $m = K_I^{ref} / \text{load step}$.

5.2.4 Variation of Material Parameters

As described in section 5.2.1, each of the modeled grains is performed with a set of material parameters deviating from an averaged value. In this contribution, we assume the different grain structures assembled of six different sets of parameters varying in the initial yield stress σ_0^I and the hardening exponent N^I , $I = 1, 2, \dots, 6$, see eqn. (5.2), while the values for YOUNGS modulus E and the POISSON number ν are fixed. Investigating different combinations of

<i>mix1</i>		<i>mix2</i>		<i>mix3</i>		<i>mix4</i>		<i>mix5</i>	
σ_0	N	σ_0	N	σ_0	N	σ_0	N	σ_0	N
460	7	480	8	464	7.2	480	7	460	8
450	5	450	6	455	6.7	450	5	450	6
470	9	480	9	468	6.5	480	9	470	9
490	11	480	9	458	7.4	480	11	490	9
400	3	440	5	463	6.8	440	3	400	5
460	7	460	7	460	7.0	460	7	460	7
455	7	465	7.33	461	6.93	465	7	455	7.33

Table 5.2: Parameters set for materials, stress dimension [MPa]; last line: averaged values

the varying sets of parameters, we define five different *mixtures*, in the following called *mix1* to *mix5*, where the initial yield stress exists in the range of $\sigma_0^I = [430, \dots, 490]$ MPa and the hardening exponent $N = [4, \dots, 11]$. Because of nearly the same portion of each material set relative to the crack tip region, one can compute the average values $\bar{\sigma}_0$ and \bar{N} by the arithmetic mean of the respective values. The chosen values for the five different mixtures are listed in Tab. 5.2 to give an overview on the referenced combinations.

5.3 Results and comparative studies for different microstructures

5.3.1 Void Growth

Several results are described in order to get an impression of the influence of the varying material parameters and the differences in the microstructure due to the coarse and the finer grain size in front of the crack tip. Fig. 5.2 shows the discretization and the coarse grain structure in the zoomed-out crack tip region. The completely discretized circular K_I -crack tip problem for the coarse substructure consists of about 33.000 nodes and over 16.000 elements, while for the discretization of the finer grains within the K_I -field over 70.000 nodes and nearly 35.000 elements are needed. Again, for the coarse grain substructure, the evolution of the plastic strain in front of the crack tip and especially around the microvoids near the ligament is plotted in Fig. 5.3 in the deformed configuration for the load steps 120, 160 and 200. Obviously, the high increased values are directly on the elongation of the existing crack tip. In Fig. 5.4, the void volume (fraction) for the different materials sets and the different grain sizes are plotted against the load level. As it can be seen, no significant differences can be found. This is explained by the displacement controlled loading, which effects just the elastic part of the volume change due to the assumption of plastic incompressibility. Fig. 5.5 shows the stress component σ_{yy} along the ligament for both discretizations at the load level 60 and 120. Additionally the near tip field solution for this stress component σ_{yy} is plotted, where not only the asymptotic behaviour but also the oscillations